

BRNO UNIVERSITY OF TECHNOLOGY

VYSOKÉ UČENÍ TECHNICKÉ V BRNĚ

FACULTY OF MECHANICAL ENGINEERING

FAKULTA STROJNÍHO INŽENÝRSTVÍ

INSTITUTE OF PHYSICAL ENGINEERING

ÚSTAV FYZIKÁLNÍHO INŽENÝRSTVÍ

PREPARATION AND CHARACTERIZATION OF ADVANCED OPTICAL METASURFACES

PŘÍPRAVA A CHARAKTERIZACE POKROČILÝCH OPTICKÝCH METAPOVRCHŮ

MASTER'S THESIS

DIPLOMOVÁ PRÁCE

AUTHOR — **Bc. Jozef Štálnik**

AUTOR PRÁCE

SUPERVISOR — **Ing. Petr Viewegh, Ph.D.**

VEDOUCÍ PRÁCE

BRNO 2026

BRNO UNIVERSITY OF TECHNOLOGY
FACULTY OF MECHANICAL ENGINEERING

Master's Thesis Assignment

Institute:	Institute of Physical Engineering
Student:	**Bc. Jozef Štálnik**
Degree programm:	Physical Engineering and Nanotechnology
Branch:	no specialisation
Supervisor:	**Ing. Petr Viewegh, Ph.D.**
Academic year:	2025/26

As provided for by the Act No. 111/98 Coll. on higher education institutions and the BUT Study and Examination Regulations, the director of the Institute hereby assigns the following topic of Master's Thesis:

Preparation and characterization of advanced optical metasurfaces

Brief Description:

Since 2016, dielectric metasurfaces represent very interesting platform for novel approaches for optical components using state–of–the–art nanotechnological procedures. However, this year scientific publications and conferences have started to present metasurfaces embedded into the substrate, which makes it possible to create two optical metasurfaces on top of each other. Mastering this latest technology for advanced optical metasurfaces would open completely unique approaches to controlling and manipulating light.

Master's Thesis goals:

1)Carry out a research study on the topic of preparation and characterization advanced optical metasurfaces.
2)Prepare and characterize optical properties of optical metasurfaces using modern state–of–the–art technological procedures.

Recommended bibliography:

DORRAH, Ahmed H.; PARK, Joon-Suh; PALMIERI, Alfonso a CAPASSO, Federico. Free-standing bilayer metasurfaces in the visible. Online. Nature Communications. 2025, vol. 16, no. 1. ISSN 2041-1723. Dostupné z: https://doi.org/10.1038/s41467-025-58205-7. [cit. 2025-10-07].

Deadline for submission Master's Thesis is given by the Schedule of the Academic year 2025/26

In Brno,

L. S.

prof. RNDr. Tomáš Šikola, CSc. Director of the Institute	doc. Ing. Jiří Hlinka, Ph.D. FME dean

Abstrakt
Cieľom tejto práce bolo vykonať rešerš na tému viacvrstvých optických metapovrchov a následne ich vyrobiť za použitia výrobnych metód na prípravu nanoštruktúr. V prvej kapitole je predstavený teoretický základ a prehľad fyzikálnych princípov dielektrických metapovrchov. V druhej kapitole je uvedená rešeršná časť pre motiváciu viacvrstvých metapovrchov. Tretia kapitola pojednáva o výrobných metódach pre prípravu jedno-vrstvých a dvoj-vrstvých metapovrchov. V poslednej kapitole sa už prezentujú výsledky výroby dvoj-vrstvých metapovrchov, kedy hlavným optimalizačným krokom bolo odstranenie polymerného rezistu. Zároveň sa tam prezentujú výsledky výroby a charakterizácie metapolarimetru.

Abstract
Main goal of this thesis was to conduct a research on multilayer optical metasurfaces and subsequently fabricate them using nanofabrication methods. The first chapter introduces the theoretical background and provides an overview of the physical principles of dielectric metasurfaces. The second chapter presents short review section motivating the study of multilayer metasurfaces. The third chapter discusses fabrication methods for the preparation of single-layer and double-layer metasurfaces. The final chapter presents the results of the fabrication of double-layer metasurfaces, where the main optimization step involved the removal of the polymer resist. In addition, the results of the fabrication and optical characterization of metapolarimeter are presented.

Kľúčové slová
dielektrický metapovrch, viacvrstvý metapovrch, dvojvrstvý metapovrch, výroba, elektrónova litografia, depozícia atomárnych vrstiev, suché leptanie

Keywords
dielectric metasurface, multilayer metasurface, bilayer metasurface, fabrication, electron beam lithography, atomic layer deposition, dry etching

ŠTÁLNIK, J. *Preparation and Characterication of Advanced Optical Metasurfaces.* Brno: Brno University of Technology, Faculty of Mechanical Engineering, 2026. 56 p., Supervisor Ing. Petr Viewegh, Ph.D.

Rozšírený abstrakt

Táto práca sa zaoberá prípravou a charakterizáciou pokročilých optických metapovrchov na báze TiO_2 nanoštruktúr. Cieľom bolo zvládnuť výrobu jednoduchých jednovrstvých metapovrchov a následne rozšíriť proces smerom k voľnostojacim dvojvrstvým metapovrchov, kde jedna vrstva stojí na druhej a okolným materiálom je vzduch.

V teoretickej časti práce je predstavený prehľad fyzikálnych princípov dielektrických metapovrchov, vrátane troch hlavných mechanizmov fázovej modulácie: propagačnej fázy, rezonančnej fázy a geometrickej (Pancharatnam-Berryho) fázy. Ďalej sú popísané konkrétne zariadenie realizované pomocou metapovrchov - metačočky a meta fázove doštičky - a napokon je zhrnutý súčasny stav výskumu viacvrstvových metapovrchových systémov.

Experimentálna časť práce popisuje celý výrobný reťazec nanoštruktúr. Ako substrát bol zvolený SiO_2 pre jeho vysokú priepustnosť vo viditeľnej oblasti spektra. Vzory nanoštruktúr boli definované elektrónovou litografiou pri urýchlovacom napätí 30 kV. Pre výrobu boli testované dva typy pozitývnych jeden bol založený na PMMA 950k AR-P 679.04 a druhý bol AR-P 6200.13 - pričom hrúbky vrstiev boli optimalizované pomocou spektroskopickej reflektometrie s cieľom dosiahnúť cýšku nanoštruktúr 500 nm. Na zlepšenie adhézie rezistu k substrátu boli testované adhézne promotéry AR 300-80 New a HMDS, pričom HMDS sa ukázal ako výrazne lepší. Pretože SiO_2 je nevodivé, na potlačenie nabíjania počas elektrónovej litografie bola použita polymérna vrstva Electra 92.

Depozícia TiO_2 bola realizovaná metódou depozície atomárnych vrstiev. Počas práce boli vzužité dva systémy. Na prvom depozičnom systéme boli zistené nezvyčajne vysoké depozičné rýchlosti, čo naznačovalo odchýlku od ideálneho samo-limitujúceho rastu. Proces bol preto presunutý na druhý systém, kde bola dosiahnutá konzistentná depozičná rýchlosť. Keďže depozícia atomárnych vrstiev deponuje materiál konformálne, výška nanoštruktúr je daná hĺbkou otvorov definovaných litografiou a nie samotnou depozíciou.

Po depozícií bola prebytočná vrstva TiO_2 na povrchu odstránená leptaním zväzkom iónov. Koncový bod leptania bol monitorovaným hmotnostnou spektroskopiou sekundárnych iónov.

Reaktívne iónové leptanie kyslíkovou plazmou spôsobovalo kolaps nanoštruktúr v dôsledku príliš agresávneho iónového bombardovania a to aj pri zníženom výkone. Problém bol vyriešený prechodom na mikrovlnné leptanie, ktoré poskytoje čisto chemické leptanie, taktiež v čisto kyslíkovej plazme.

Po optimalizácií procesu pre jednu vrstvu bol realizovaný pokus o výrobu voľnostojacich dvojvrstvých TiO_2 metapovrchov. Kľúčovým princípom tejto architektúry je selektívny vývin rezistu vo vývojke. Čo umožnilo vyvinuť vzor v druhej vrstve rezistu bez porušenia spodného rezistu. Celý výrobný proces

bol potom v podstate dva cykly toho istého procesu s tým, že v druhom cykle sme využili druhý typ rezistu. Pre presné trafenie vzoru pre hornej vrstvy na tú spodnú, boli v dizajne pridané zameriavacie kríže, ktoré slúžili ako globálne a lokálne zarovnávacie značky, pričom sa ukázalo že značky vytvorené z TiO_2 sú dostatočne viditelné aj pod vrstvou druhého rezistu. Toto zistenie nám umožnilo úplne vynechať dodatočný kroky pre vytvorenie značiek z napr. kovu. Napokon sa výrobný proces voľnostojacich dvojvrstvých metapovrchov na báze TiO_2 skúmaný v tejto práci usvedčil, pretože takéto štruktúry sa podarilo vytvoriť.

Paralelne s výrobou dvojvrtsvého metapovrchu bol úspešne vyrobený a opticky charakterizovaný aj jednovrstvový polarimeter. Toto zariadenie kombinuje funkcie metačočy a vlnovej doštičky s fázovym posunom $3\pi/4$. Metapolarimeter pozostáva z obdĺžnikových nanoštruktúr z TiO_2. Optická charakterizácia bola prevedená na vlastnej optickej zostave. Meraním bolo zaznamenané rozloženie rozptylovej funkcie, ktorá má charakteristický tvar podľa typu polarizácie dopadajúceho svetla na metapolarimeter. Následne sa z meraní zrekonštruovali stokesové parametre chyba rekonštrukcie k teoretickým simuláciam bola menšia ako 3%, čo potvrdzuje správnu optickú funkčnosť.

I hereby declare that I wrote this diploma thesis by myself under the supervision of Ing. Petr Viewegh, Ph.D. All sources and references are cited in the List of References section. This work was created with the help of generative AI models ChatGPT and ClaudeAI, which was used for publication research, text formating, grammatical corrections and correction of structure of the text. In case of using AI, the generated text has been reviewed and checked, and I take full responsibility for the text in the thesis.

Bc. Jozef Štálnik

Poďakovanie

Týmto by som chcel poďakovať všetkým, ktorí mi pomohli pri vypracoví tejto práce. Osobitne by som chcel poďakovať môjmu vedúcemu Ing. Petrovi Vieweghovi, Ph.D za konzultácie, cenné rady, odborné vedenie a namä za voľnosť, ktorú mi poskytol. Zároveň by som mu chcel poďakovať za pomoc pri charakterizácií vyrobených metapovrchov. Najviac by som chcel poďakovať Ing. Beáte Idesovej za užitočné rady pri výrobe, ale najmä za korektúru textu tejto práce. Moje poďakovanie patrí aj Ing. Ondřejovi Červinkovi za pomoc so spracovaním nameraných výsledkov a Ing. Martinovi Hrtoňovi Ph.D. za poskytnutie vzoru funkčného metapovrchu. Chcel by som ešte poďakovať Bc. Radimovi Slovákovi a Bc. Lukášovi Koňaříkovi za príjemné chvíle v laboratóriu, vďaka ktorým bolo aj pri neúspechoch vždy dôvod sa zasmiať. Na záver by som chcel poďakovať svojej rodine a priateľom za podporu, trpezlivosť a povzbudenie počas celého štúdia.

Táto práca bola realizovaná za podpory výskumnej infraštruktúry CzechNanoLab (ID 90251), financovanej Ministerstvom školstva, mládeže a telovýchovy ČR.

Bc. Jozef Štálnik

Contents

Introduction **3**

1 Theory **5**
1.1 Plasmonic metasurfaces 5
1.2 Dielectric metasurfaces 6
1.3 Phase manipulation in dielectric metasurfaces 6
1.3.1 Propagation and resonant phase mechanisms 7
1.3.2 Geometric phase mechanism 8
1.4 Metalenses 9
1.5 Meta wave plates 10

2 Multilayer Metasurfaces **13**

3 Experimental Methods **15**
3.1 Electron beam lithography 15
3.2 Atomic layer deposition 17
3.3 Dry etching techniques 18
3.3.1 Reactive ion etching 18
3.3.2 Ion beam etching 20
3.3.3 Microwave etching 22

4 Results **23**
4.1 Optimization of fabrication 23
4.1.1 Preparation of samples 23
4.1.2 Bilayer metasurface fabrication 32
4.2 Metapolarimeter 38
4.2.1 Design and fabrication 38
4.2.2 Optical measurements 39

Conclusion **45**

List of Abbreviations **47**

List of References **49**

Introduction

In the effort to push the boundaries of optical technologies, classical optics faces natural limitations. Conventional optical components, constrained by the diffraction limit and their physical size, struggle to keep pace with the ever-growing demand for miniaturization and more compact devices. Advances in nanofabrication have enabled the creation of structures capable of controlling light in ways that were previously not possible, giving rise to planar photonics and a new class of optical components known as metasurfaces.

Metasurfaces have emerged as revolutionary platforms in the field of electromagnetic wave manipulation, offering unprecedented control over the properties of light. These artificially engineered two-dimensional structures have captivated the scientific community with their ability to shape wavefronts, control polarization, and induce exotic optical phenomena (see Figure 1) [1, 2].

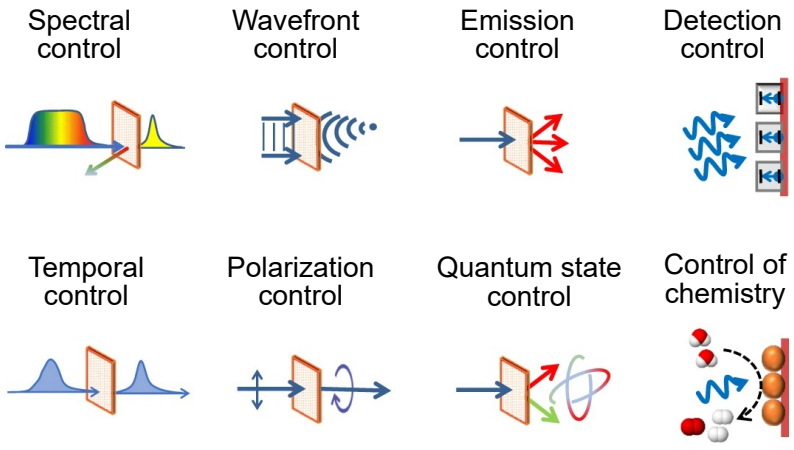


Figure 1: Portfolio of possible functions of metasurfaces. Adapted from [3].

Optical metasurfaces exploit local modifications of the phase response of transmitted or reflected light, offering a fundamentally different approach to optical manipulation compared to conventional optical elements [4]. These wavefront modifications are achieved through scattering by resonant metallic or dielectric nanostructures, commonly referred to as meta-atoms or building blocks [5]. Since the lateral dimensions of these nanostructures are well below the diffraction limit of

the incident light, metasurfaces can exhibit unique optical properties unattainable by conventional optics [6].

However, achieving multiple optical functionalities simultaneously within a single metasurface layers IS challenging, as independent control over all properties of light often requires compromises in efficiency or bandwidth. This has motivated the development of multilayer and bilayer metasurface architectures, where different optical functionalities are distributed across vertically stacked layers, enabling more sophisticated light manipulation while preserving the compact planar form that makes metasurfaces attractive in the first place.

1. Theory

Metasurfaces are two-dimensional arrays of subwavelength artificial structures, commonly referred to as meta-atoms, which enable precise control over the amplitude, phase and polarization of electromagnetic waves [7–12]. Unlike conventional optical components that rely on gradual phase accumulation during propagation through bulk materials, metasurfaces achieve wavefront shaping through abrupt phase discontinuities introduced at an interface. Each meta-atom acts as an individual scatterer whose response depends on its geometry, material composition and local environment. Spatial variations of these parameters across the surface enables engineering of arbitrary phase profiles [13]. This allows functionalities such as beam steering [14], focusing [15–17], holography[18–20] and polarization control [21].

Based on the material platform, metasurfaces can be broadly classified into plasmonic and dielectric types. Which will be more explained in the next chapter.

1.1 Plasmonic metasurfaces

Plasmonic metasurfaces utilize metallic nanoantennas that support localized surface plasmon resonances [22]. At resonance, the incident electromagnetic field drives coherent oscillations of free electrons, leading to strong localization and enhancement of the electric field in the vicinity of nanostructure [23]. This strong field localization enhances light-matter interaction, which allows for efficient modification of the amplitude and phase of scattered light. The resonant response of each nanoantenna is highly dependent on its geometry, material properties and surrounding dielectric environement. As a result, the spectral position and strength of the resonance can be tuned, enabling control over phase delay and scattering characteristics of the transmitted or reflected wave. Plasmonic platforms enabled some of the first experimentally realized metasurfaces capable of arbitrary wavefront shaping and demonstrated functionalities such as anomalous reflection and refraction, beam steering and holography [24–27]. Despite these advantages, plasmonic systems suffer from significant ohmic losses originating from absorption within the metal. As a result, part of the electromagnetic energy is dissipated as heat, limiting the transmission efficiency and overall performance of plasmonic metasurfaces,

particularly in the visible and near-infrared spectral regions [28]. This absorption of energy is particularly significant in the visible and near-infrared spectral regions, which severely limits the efficiency and practical applicability of plasmonic metasurfaces in these wavelength ranges. To overcome these limitations, dielectric metasurfaces based on high-refractive index, low-loss materials have emerged as a compelling alternative.

1.2 Dielectric metasurfaces

To overcome the limitations associated with metallic nanostructures, dielectric metasurfaces based on high-refractive-index and low-loss materials have emerged as a low-loss platform for high efficiency wavefront control [29]. Commonly used materials include silicon [30], oxides [31, 32] and nitrides [33], which exhibit low optical absorption while maintaining strong electromagnetic field localization [34].

The fundamental building blocks of dielectric metasurfaces are subwavelength high-index nanoantennas whose optical response is determined by their interaction with the incident electromagnetic field. Depending on their geometry and arrangement, dielectric nanoantennas can operate through several physical mechanisms, including electric and magnetic Mie resonances, waveguide-like modes or hybrid regimes combining both effects [35]. This versatility allows tuning of the spectral and polarization response of transmitted or reflected light while maintaining low absorption losses and high optical efficiency [36].

1.3 Phase manipulation in dielectric metasurfaces

Arbitrary wavefront shaping with metasurfaces requires phase control spanning the full 2π range. Spatially varying phase profiles enable functionalities such as beam steering, focusing, holography and polarization manipulation [1]. In dielectric metasurfaces, phase control is achieved by tailoring the interaction of incident light with meta-atoms through three main mechanisms: propagation phase, resonant phase and geometric phase.

Propagation phase originates from the phase delay accumulated as light propagates through the nanoantennas. Resonant phase metasurfaces rely on localized electric and magnetic resonances supported by the individual meta-atoms. First two method are dependent on meta-atoms geometry, in contrast, geometric phase metasurfaces utilize polarization conversion induced by rotated anisotropic structures.The ability to engineer the optical response of individual meta-atoms forms the foundation for precise phase control across the metasurface, which will be discussed in the following section.

1.3.1 Propagation and resonant phase mechanisms

Propagation phase arises from the accumulated phase inside meta-atoms and depends on their geometry and material properties. Several physical regimes can be distinguished depending on the metasurface parameters. For metasurfaces with small lattice periods relative to wavelength, neighboring nanoposts are strongly coupled and each meta-atom can be approximated as a truncated dielectric waveguide. The incident electromagnetic field excites guided modes inside the nanopost, resulting in phase accumulation determined primarily by effective refractive index of these modes. In this regime, the nanopost behaves similarly to a low-quality-factor Fabry-Pérot resonator as shown by [37–39].The accumulated phase can be then approximated by:

$$\Phi \approx \frac{2\pi}{\lambda} n_{\mathrm{eff}} h, \tag{1.1}$$

where λ is the free-space wavelength, n_{eff} is the effective refractive index of the guided mode and h is the height of the nanopost. By varying the lateral dimensions of the nanopost, the effective refractive index changes, enabling continuous phase tuning. This mechanism is illustrated in Figure 1.1(a,c).

As the lattice period increases, the coupling between neighboring nanoposts becomes weaker and the optical response becomes dominated by localized resonances within the individual nanoantennas. In this regime, phase control originates from electric and magnetic dipole resonances, commonly referred to as Mie resonances. Each resonance contributes approximately a π phase shift [40]. When the electric and magnetic dipole resonances spectrally overlap, their combined response enables full 2π phase coverage while maintaining high transmission efficiency [8, 41, 42]. This condition is commonly associated with Huygens metasurfaces [43], where constructive interference between electric and magnetic response suppresses backscattering and enhances forward transmission. The resonant phase mechanism based on electric and magnetic dipole resonances is illustrated in Figure 1.1(b,d).

Between the Fabry-Pérot and Mie resonance regimes, an intermediate transition region exists in which the optical response cannot be attributed to a single dominant mechanism. Instead, both waveguide-like propagation effects and localized resonant scattering contribute simultaneously to the phase response. Li et al. [35] showed that the phase behavior becomes more complex and less predictable compared to the pure Fabry-Pérot and Mie regimes. Although complete 2π phase coverage can still be achieved, the optical response in this regime is generally more sensitive to geometrical variations and fabrication tolerances, which complicates practical metasurface design.In contrast to the phase and resonant mechanism discussed above, which all rely on tailoring the geometry of individual meta-atoms, the geometric phase mechanism exploits the spatial rotation of

anisotropic nanostructures to achieve phase control, as described in the following section.

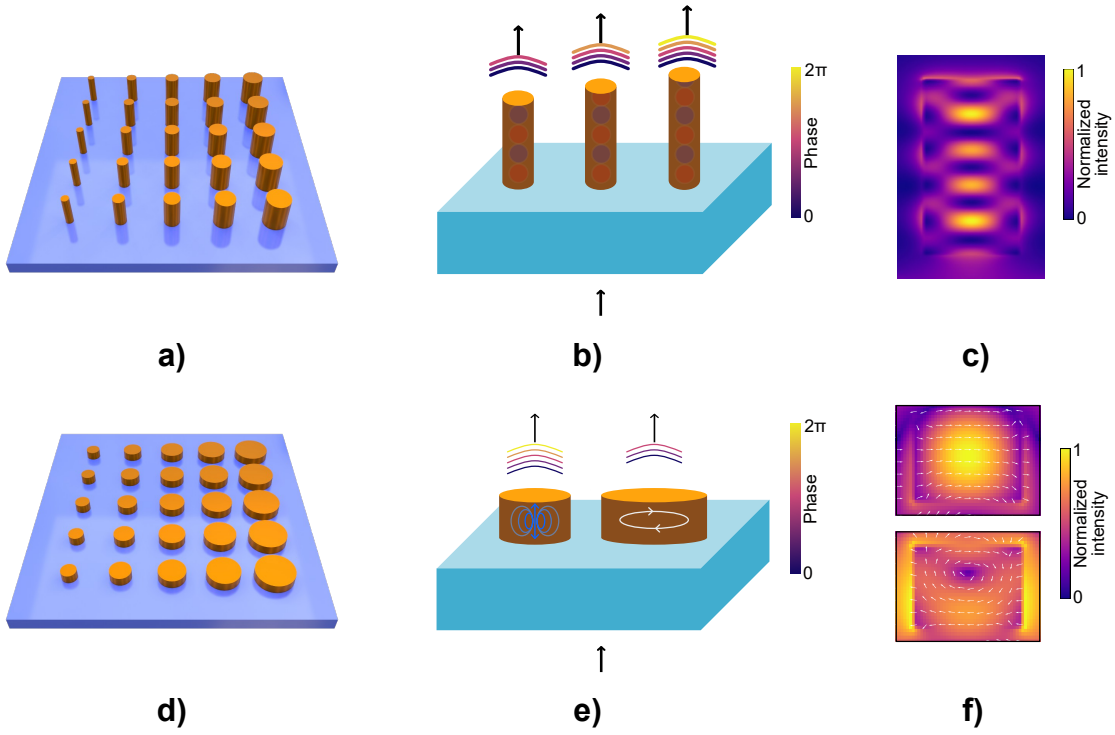


Figure 1.1: Schematic comparison of propagation-phase and resonant-phase mechanisms in dielectric metasurfaces. (a-c) Propagation-phase regime in high-aspect-ratio nanoposts. Phase control is achieved through approximation of nanoposts as low-quality Fabry-Pérot resonators, where varying the nanopost diameter modifies the effective refractive index and accumulated optical phase. (a) Metasurface composed of high-aspect-ratio nanoposts with different diameter. (b) Illustration of resonator modes inside nanoposts and corresponding transmitted phase shifts. (c) Simulated near-field intensity distribution of the cavity mode inside silicon nanopost. (d-f) Metasurface composed of low-aspect-ratio nanodisks with varying diameters. (e) Schematic illustration of electric and magnetic dipole resonance and corresponding phase shifts. (f) Simulated near-field intensity distributions associated with electric dipole (top) and magnetic dipole (bottom) resonances.

1.3.2 Geometric phase mechanism

In addition to the propagation-based and resonant-based phase control, dielectric metasurfaces can also employ geometric phase, commonly referred to as Pancharatnam-Berry phase (PB-phase). In this case, the phase shift is determined by the in-plane rotation of anisotropic nanoantennas rather than by their resonant response. When circularly polarized light interacts with a rotated anisotropic

meta-atom, such as a nanofin or rectangular nanopost, the transmitted light acquires an additional phase shift proportional to twice the rotation angle [44, 45]:

$$\Phi_{PB} = \pm 2\theta, \tag{1.2}$$

where θ is the rotation angle of the nanoantenna and the sign depends on the handedness of the incident circular polarization. The resulting phase shift has a geometric origin associated with the evolution of the polarization state on the Poincaré sphere [46]. A major advantage of the geometric phase approach is that complete 2π phase coverage can be achieved simply through rotation of identical structures, simplifying metasurface design and fabrication. However, this mechanism inherently depends on the polarization state of the incident light and is therefore typically limited to polarization-dependent applications, such as vector vortex beam generation [47] or metaholography [48]. A schematic representation of the geometric phase mechanism together with representative nanofin-based metasurface implementations is shown in Figure 1.2.

Building upon the phase manipulation capabilities of dielectric metasurfaces, we can now begin to assemble real metasurface devices.

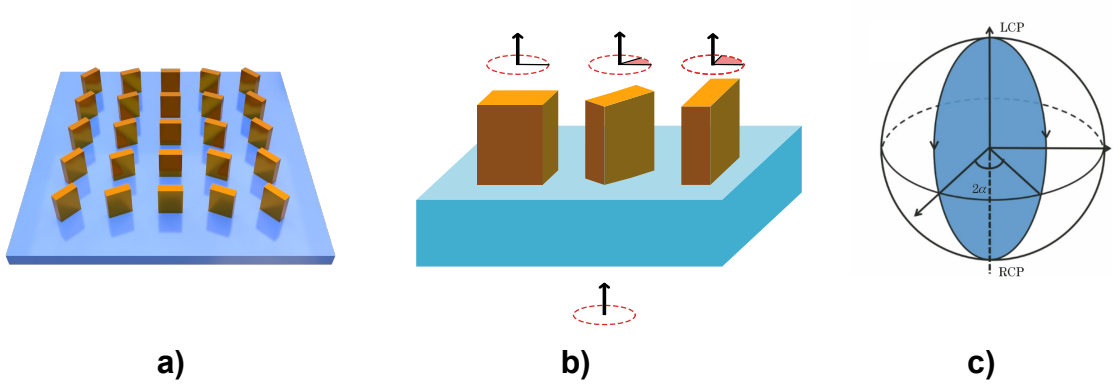


Figure 1.2: Geometric-phase mechanism in dielectric metasurfaces. (a) Metasurface composed of anisotropic nanoantennas with spatially varying in-plane orientation. (b) Phase control achieved through rotation of anisotropic meta-atoms, where the transmitted phase is determined by the rotation angle under circularly polarized illumination. (c) Schematic representation of the geometric phase on the Poincaré sphere associated with polarization-state evolution. Adapted from [49].

1.4 Metalenses

Metalenses utilize spatially varying phase distributions to control the propagation of light within an ultra-thin planar structure. Unlike conventional refractive lenses, which rely on the gradual phase accumulation during propagation through bulk

material, metalenses shape the optical wavefront by locally imposing the required phase shift at the metasurface interface. To focus an incident plane wave into a focal point located at distance f, the metasurface must transform the incoming planar wavefront into a converging spherical wavefront. This requires a spatially varying hyperbolic phase profile given by:

$$\Phi(x,y) = -\frac{2\pi}{\lambda}(\sqrt{x^2 + y^2 + f^2} - f), \tag{1.3}$$

where λ is the operating wavelength, x and y are inplane position of meta-atoms, and f is the focal length of the metalens [50]. This phase profile represents the optical path difference between the center and an arbitrary position (x,y) on the metasurface. In practical implementations, the continuous phase distribution is discretized into an array of subwavelength meta-atoms, each designed to impart a specific local phase delay. The required phase response is achieved by appropriately tuning the geometrical parameters of the individual nanoantennas, such as their diameter, width, or height. In dielectric metalenses, phase control is most commonly achieved through mechanisms associated with Mie-type resonances or waveguide-like modes supported by high-index nanoposts, which were mentioned in previous chapter. By engineering the dimensions of these structures, it is possible to achieve 2π phase coverage while maintaining high transmission efficiency. Such principle can be seen in the Figure. 1.3.

1.5 Meta wave plates

Wave plates are optical elements that converts one polarization state of the art into another by introducing a phase delay between two orthogonal polarization components [51, p. 248]. Conventional wave plates rely on birefringence materials, where the refractive index depends on the polarization direction of the incident light [52, p. 388]. As a result, orthogonal polarization components accumulate different optical phases during propagation through the material. The resulting phase retardation is then given by:

$$\Delta\phi = \frac{2\pi}{\lambda}(n_x - n_y)d, \tag{1.4}$$

where n_x and n_y are refractive indices for the orthogonal polarization directions, d is thickness of the birefringent material, and λ is the wavelength of the incident light. Depending on the introduced phase difference, different polarization transformations can be achieved. For example, a half-wave plate introduces a phase retardation of π, while a quarter-wave plate produces a retardation of $\pi/2$.

Similarly to metalenses, metasurface provide an alternative to conventional bulk waveplates by engineering the optical response at the subwavelength scale.

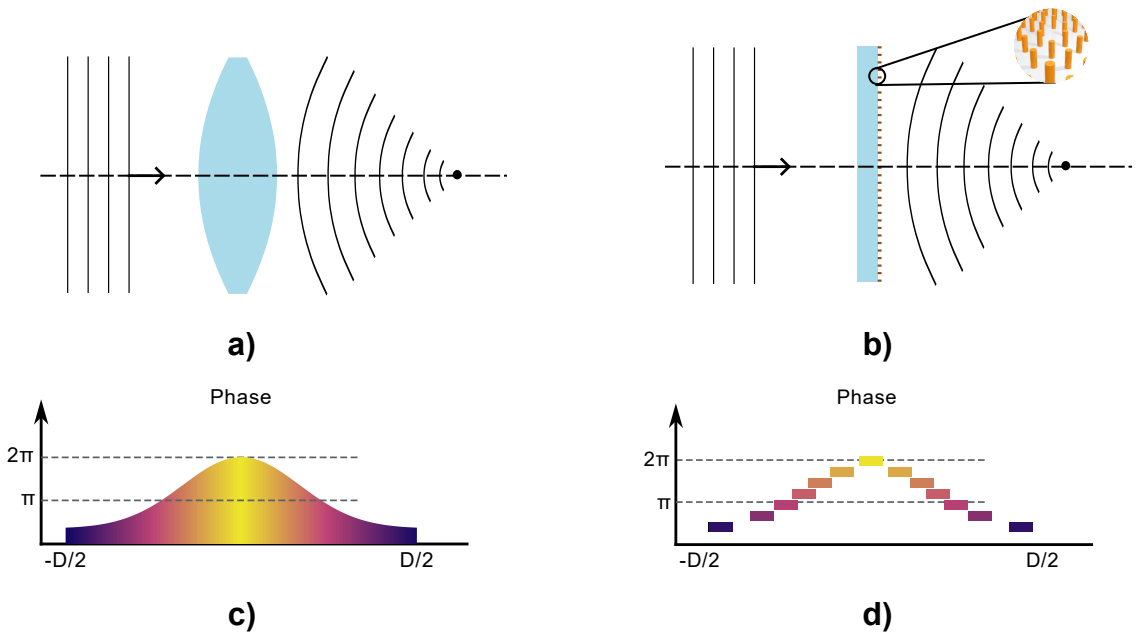


Figure 1.3: Comparison of wavefront shaping in conventional refractive lens and metalens. (a,b) Focusing of an incident plane wave using a conventional refractive lens (a) and a metasurface lens composed of subwavelength meta-atoms providing spatially varying phase shifts (b). (c,d) Corresponding continuous and discretized phase profiles required for wavefront shaping in conventional optics (c) and metasurfaces (d).

In metasurfaces, waveplate functionality is typically achieved using anisotropic meta-atoms, such as rectangular nanofins or elliptical nanoposts, which exhibit different effective refractive indices for orthogonal polarization directions[53, 54]. By carefully designing the geometry of these nanostuctures, it is possible to achieve the required phase retardation. When anisotropic meta-atom is specifically designed to introduce a phase retardation of π between orthogonal axes - effectively acting as half-wave plate - the geometric phase mechanism becomes particularly powerful. In that case, complete 2π phase coverage can be achieved purely through rotation of the nanostructures, without any need to vary their geometry. This combination of propagation and geometric phase control forms the operating principle of many practical metasurface devices.

2. Multilayer Metasurfaces

Despite the remarkable capabilities of single-layer metasurfaces, simultaneously controlling multiple optical properties within a single planar layer remains challenging. In particular, achieving independent manipulation of wavelength, polarization, phase or amplitude often requires compromises in efficiency, bandwidth or overall device functionality. As a result, multilayer and bilayer metasurfaces emerged as a promising approach for extending the achievable optical response while preserving the compact planar nature of metasurface optics. By vertically stacking multiple metasurface layers, different optical functionalities can be distributed between individual layers, enabling more sophisticated manipulation of light than is typically possible with conventional single-layer designs.

One of the early demonstrations of multilayer metasurfaces was presented by Avayu et al. [55], who proposed cascaded metasurface layers fabricated from different materials and independently engineered for distinct spectral bands. Their multilayer design enabled spectral multiplexing and chromatic aberration correction by combining several metasurface layers into a single ultrathin optical element. The authors experimentally realized a multispectral achromatic metalens operating for red, green and blue light. The work was among the first studies to highlight the potential of multilayer metasurfaces. Building on this concept, later works explored increasingly sophisticated layered meta-optical systems from multifunctional operation. Zhou et al. [56] showed that stacked dielectric metasurfaces can simultaneously manipulate optical properties, enabling multiwavelength metaholograms, wavelength-selective waveplates and polarization insensitive holograms with simultaneous phase and amplitude control. These results demonstrated the broader functionality accessible through bilayer architectures. More recently, Deng et al. [57] demonstrated bilayer metasurfaces capable of independent wavefront manipulation in both transmission and reflection. By using cascaded anisotropic nanofins based on PB-phase mechanism, the authors experimentally realized multifunctional devices such as trans-reflective metaholograms and vortex beam generators operating in the visible spectral range.

A major recent advancement in multilayer meta-optics was demonstrated by Dorrah et al. [58], who introduced free-standing bilayer metasurfaces operating in the visible regime. Unlike previous multilayer designs relying on substrates, cladding

layers or separated stacked structures, their approach utilized vertically stacked TiO_2 nanofins surrounded by air. This configuration provided high-refractive index contrast, reduced parasitic reflections and stronger optical confinement. The underlying theoretical framework for such bilayer structures was further clarified by Palmieri et al. [59], who investigated the conditions under which layers may be approximated as decoupled single-layer metasurfaces. Their analysis showed that near-field coupling can become negligible provided that the meta-atoms operate away from strong resonances and have appropriate dimension (with bottom meta-atom larger than the upper one) allowing the overall response to be modeled through cascaded Jones matrices. Using these principles, Dorrah et al. demonstrated geometric-phase metasurfaces capable of manipulating linearly polarized light through cyclic polarization evolution on the Poincaré sphere. This approach extended the conventional PB-phase concept beyond operation solely under circular polarized illumination.

For me, the free-standing architecture is particularly interesting as it maximizes index contrast and minimizes parasitic optical interactions, representing what is arguably the most optically clean realization of multilayer metasurface. Unfortunately, such structures have not yet been fabricated at our institute, and exploring their realization in our facilities is one of the central motivations of the present work. The following chapter describes the experimental methods and nanofabrication techniques employed throughout this work to work towards this goal.

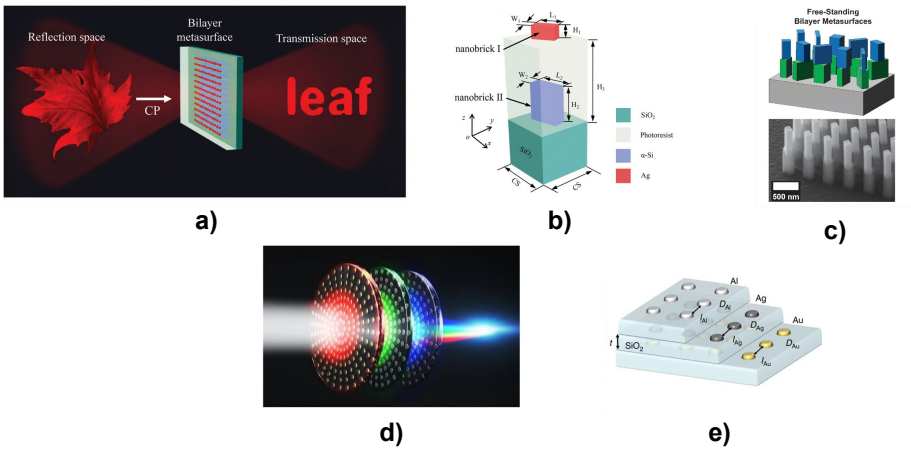


Figure 2.1: Representative multilayer metasurface architecture and functionalities. (a,b) Bilayer metasurface for full-space meta-holography enabling independent holographic images in transmission and reflection together with corresponding unit-cell design composed of stacked metallic and dielectric nanobricks. (c) Free-standing bilayer dielectric metasurface and corresponding SEM image. A (d,e) Cascaded multilayer metasurfaces for spectral multiplexing shown as conceptual illustration (d) and schematic representation of the multilayer architecture (e). Figures are adapted from [55, 57, 58].

3. Experimental Methods

3.1 Electron beam lithography

In electron beam lithography (EBL) a focused beam of electrons is used as the exposure source, enabling fabrication of structures with nanometer-scale resolution. This chapter is based on following literature [60, 61].

Unlike conventional optical lithography, which relies on electromagnetic radiation, EBL employs accelerated electrons as the writing source. This eliminates the need for photomasks and enables direct writing of arbitrary patterns with extremely high resolution. The electron beam is focused by electromagnetic lenses to a spot size of a few nanometers and scanned across the substrate in controlled manner, allowing fabrication of structures with dimensions approaching ≈10 nm. The minimum achievable spot size is determined by the diffraction limit, which in the case of electrons depends on the accelerating voltage - higher voltages yield shorter de Broglie wavelengths and therefore smaller spot sizes. The achievable resolution in EBL is mainly determined by the interaction of the incident electrons with both resist and substrate material. As electrons penetrate the sample, they undergo multiple elastic and inelastic scattering events, leading to broadening of the exposed region inside the resist. Forward scattering inside the resist slightly increases the beam diameter, while backscattered electrons originating from the substrate can expose nearby regions surrounding the intended pattern. This phenomenon, commonly referred to as proximity effect, becomes particularly important for nanostructures with small periodicity, such as metasurfaces. The magnitude of the proximity effect strongly depends on the acceleration voltage, resist thickness, substrate material, and pattern density. Higher acceleration voltages generally reduce forward scattering and improve resolution, but also increase the penetration depth of the electrons into the substrate. For dielectric substrates, an additional complication arises from charge accumulation during exposure, which can locally deflect the electron beam and distort the written pattern.

Although EBL offers exceptional resolution and flexibility, its serial writing process results in low throughput and long exposure times, making it more suitable for prototyping and research applications. A key component of the process is the

resist, a thin polymer layer applied on the substrate, typically by spin-coating, with thicknesses ranging from tens to hundreds of nanometers, depending on what is your next step after lithography. The choice of resist and exposure conditions strongly influences the final pattern quality. Resist used in EBL are commonly classified as positive or negative. In positive resists, electron exposure breaks polymer chains, which increases the solubility in the developer, resulting in removal of exposed areas. In contrast, negative resists undergo cross-linking upon exposure, which reduces the solubility in the developer resulting in removal of unexposed areas. Schematic illustration of development of patterned structure on positive and negative resist is shown in Figure 3.1.

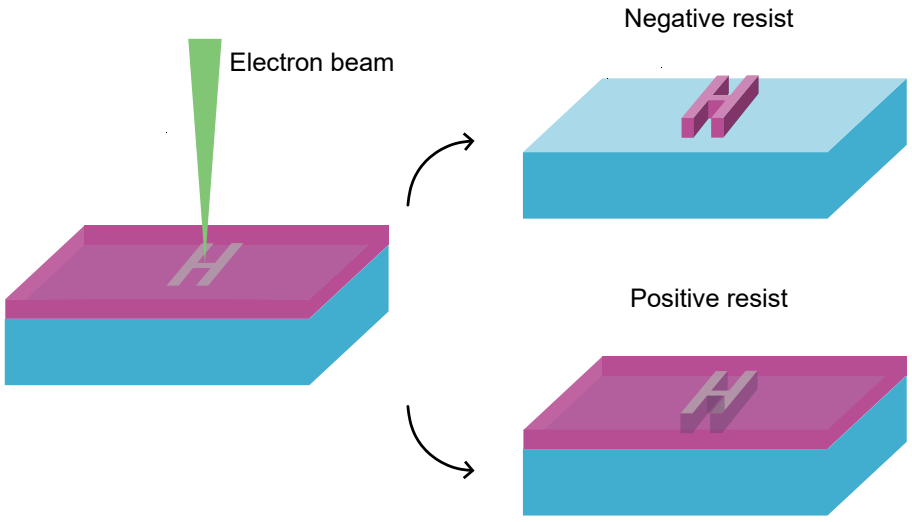


Figure 3.1: Schematic illustration of the electron beam lithography process using negative and positive resists. In the negative resist process (top), the exposed regions become insoluble after electron exposure and remain on the substrate after development. In the positive resist process (bottom), the exposed regions become soluble and are removed during development, leaving behind the desired pattern.

In addition to the resist properties, the exposure parameters play a crucial role in defining the final structures. The electron dose determines the amount of energy delivered to the resist and must be carefully optimized to achieve the desired pattern without under- or overexposure. Insufficient dose can lead to incomplete development, while excessive dose may result in feature broadening and loss of resolution, particularly in dense periodic structures affected by proximity effect. Another important parameter is write field size, which defines the area that can be exposed without stage movement. Large patterns are divided into multiple write fields and stitching between them can introduce alignment errors that affect pattern continuity and accuracy. Although smaller write fields generally reduce beam deflection errors and improve patterning accuracy within a single field, they also increase the number of stitched fields required for larger structures.

With the exposure parameters established, the next step in the fabrication process was the deposition. While multiple deposition techniques exist, atomic layer deposition was selected for this purpose, as its conformal and self-limiting growth mechanism makes it particularly well suited for the fabrication of high aspect ratio nanostructures with precise thickness control.

3.2 Atomic layer deposition

Atomic layer deposition (ALD) is a thin-film deposition technique that enables precise control of the film thickness at the atomic scale. It is based on sequential, self-limiting surface reactions between gaseous precursors and substrate, allowing for highly uniform and conformal coatings [62]. The ALD process consists of repeated cycles, each involving two or more precursor exposures separated by purge steps. In typical cycle, the first precursor, let us call it precursor A, is introduced into the reaction chamber, where it adsorbs onto the substrate surface by reacting with available active sites (usually -OH groups). This reaction is self-limiting, meaning that once all reactive surface sites are occupied, no further adsorption occurs. In next step, an inert gas (typically nitrogen or argon) is used to purge excess precursor A and any gaseous by-products from the chamber, preventing unwanted gas-phase reactions. Then, the second precursor, let us call it precursor B, is introduced and reacts with the surface species created during the first step. This reaction forms a thin layer of the desired material while regenerating reactive sites for the next cycle. At last, second purge removes excess precursor B and reaction by-products, completing full ALD cycle. The process is schematically illustrated in Figure 3.2. The quality and uniformity of ALD films strongly depend on precise timing of the individual process steps. The precursor pulse duration must be sufficiently long to ensure complete saturation of all available surface sites. On the other hand, excessively long pulses do not increase the growth rate and may lead to unnecessary precursor consumption. Similarly, the purge time between precursor exposure must be carefully optimized to fully remove excess precursor molecules and reaction by-products from the chamber. If the purge time is not optimized and the purge is insufficiently long it causes pulse overlap [63]. Insufficient purging can result in unwanted gas-phase reactions between the precursors, leading to non-uniform growth and degradation of film quality. In addition, the deposition temperature must remain within the so-called ALD window, where the surface reactions preserve their self-limiting behavior. Outside the ALD window, precursor condensation or thermal decomposition may occur, negatively affecting the growth process and film properties [64]. The growth per cycle is typically on the order of fraction of nanometer and depends on the specific precursor chemistry and process conditions, such as temperature and pressure. The process is usually carried out within a specific

temperature window, known as the ALD window, in which the growth rate remains constant. Common materials deposited by ALD include oxides as Al_2O_3, HfO_2 and TiO_2, nitrides and metals [62, 63].

ALD processes can be distinguished by mechanism that drives the surface reactions on thermal ALD and plasma-enhanced ALD. In thermal ALD, the reactions are driven purely by thermal energy, requiring the sample to be helds at sufficiently large temperature. In plasma-enchanced ALD, a plasma is used to generate reactive radicals that can drive surface reactions at lower temperatures.

Despite its advantages, however, ALD is relatively slow compared to other deposition techniques due to its cyclic nature. But its thickness control, uniformity and conformal deposition ability make it really suitable for metasurface nanofabrication. Once the material is deposited the desired nanostructures must still be physically defined, this task is typically accomplished through dry etching techniques.

3.3 Dry etching techniques

Dry etching techniques are widely used in micro- and nanofabrication for controlled material removal and surface modification. In contrast to wet chemical etching, dry etching processes are typically plasma-based and provide improved anisotropy, pattern transfer fidelity and compatibility with nanoscale fabrication [65]. Depending on the dominant mechanism, dry etching techniques may rely on chemical reactions, physical bombardment or combination of both effects. Among the plasma-based dry etching techniques, reactive ion etching was investigated for resist removal due to its ability to selectively etch organic materials using oxygen plasma.

3.3.1 Reactive ion etching

Reactive ion etching (RIE) is plasma-based dry etching technique used for controlled and anisotropic material removal from substrate. The process combines chemical reactions with directional ion bombardment, enabling precise pattern transfer in micro- and nanofabrication [66, 67]. The process takes place in vacuum chamber where a process gas is introduced and ionized by an applied radio-frequency electric field forming a plasma. Schematic illustration of chamber is shown in Figure 3.3. This plasma contains mixture of ions, electrons and neutral reactive species, called radicals. Although electrically neutral, these radicals are highly chemically reactive due to their unpaired valence electron. Due to the high mobility of electrons compared to ions in the radio-frequency electric field, a negative DC self-bias is formed at the substrate surface. As a result, positive ions are accelerated toward

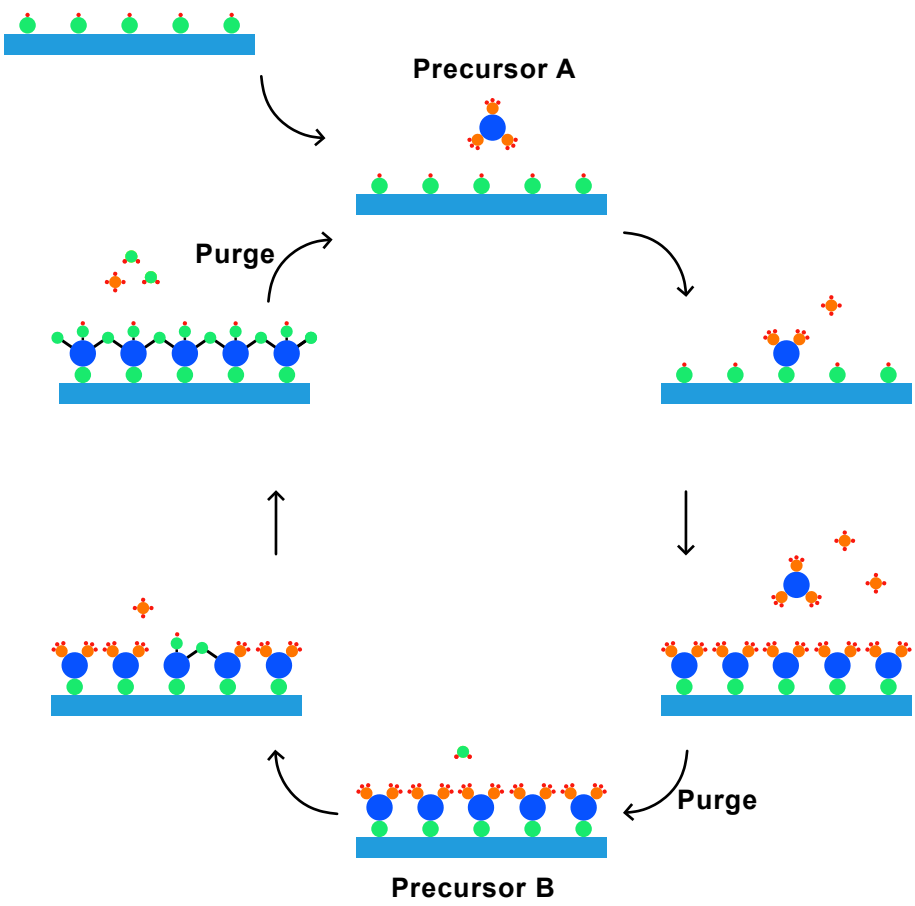


Figure 3.2: Schematic illustration of a single atomic layer deposition (ALD) cycle. During the first half-cycle, precursor A is introduced into the chamber and reacts with the available reactive sites on the substrate surface. The reaction proceeds until all available surface sites are occupied, resulting in a self-limiting process. Excess precursor molecules and reaction by-products are subsequently removed during the purge step. In the second half-cycle, precursor B reacts with the surface species formed during the first step, creating a thin layer of the desired material while regenerating reactive surface sites. A second purge step removes the remaining precursor molecules and reaction by-products, completing one ALD cycle.

the substrate with significant energy, primarily in a direction perpendicular to the surface [68, 69]. These energetic ions subsequently participate in the etching process together with radicals. For this reason material removal in RIE occurs through two different mechanisms. The first is chemical etching, where reactive radicals interact with the substrate material to form volatile compounds. The second is physical sputtering, where energetic ions bombard the surface enhancing the removal of material. The combination of these effects allows for efficient and controllable etching.

The etching characteristics depend on several parameters. The gas composition determines the chemistry of the reactive species and therefore the chemical selectivity towards the etched material - for example, fluorine-based gases such as SF_6 are commonly used for silicon etching [66], chlorine-based gases tend to be preferred for

metals [70] and oxygen-based for organic compounds [71]. The chamber pressure affects the mean free path of the ions and radicals - lower pressures lead to more directional ion bombardment and better anisotropy, while higher pressures favor chemical etching and make the process more isotropic. The RF power controls the density of the plasma and the flux of reactive species, which directly affects the etch rate. The substrate bias then controls the energy of the ions hitting the substrate - higher bias increase the physical sputtering, which improves anisotropy and allows etching of materials that would otherwise be chemically resistant. By adjusting these parameters, it is possible to control the etch rate, selectivity and anisotropy of the process.

While RIE combines chemical and physical mechanisms to achieve selective and anisotropic etching, material removal can also be realized through purely physical sputtering processes such as ion beam etching.

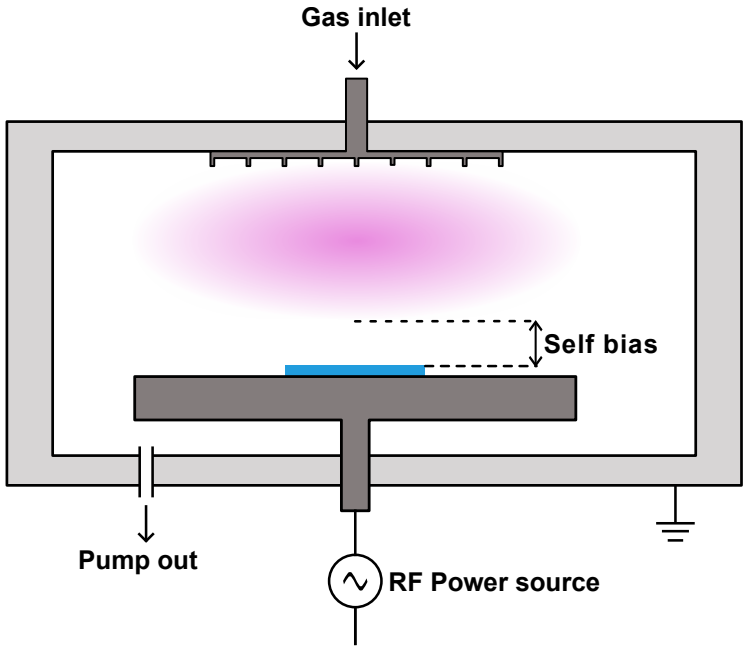


Figure 3.3: Schematic illustration of the reactive ion etching process. A process gas is introduced into the vacuum chamber and ionized by an applied radio-frequency (RF) electric field, forming a plasma containing ions and reactive species. Due to the formation of a negative DC self-bias at the substrate surface, positively charged ions are accelerated toward the sample, where the combined effect of chemical reactions and ion bombardment enables anisotropic material removal.

3.3.2 Ion beam etching

Ion beam etching (IBE), also referred to as ion milling, is a physical dry etching technique based on the sputtering of material from a substrate by energetic ions of inert gases. In contrast to RIE, IBE relies primarily on momentum transfer rather than chemical reactions.

In IBE process, ions are generated in a separate ion source and accelerated toward the substrate in the form of a directional beam [72]. In most cases, inert gases such as argon are used to avoid chemical interactions with the substrate. The ions are accelerated by an electric field onto the sample surface. When the energetic ions strike the substrate, they transfer momentum to surface atoms, causing them to be ejected from the material. Schematics of this mechanism can be seen in Figure 3.4. This process leads to material removal. Since the mechanism is purely physical, IBE can be used to etch wide range of materials, including those that are chemically inert or difficult to process using reactive plasmas. A key feature of ion beam etching is the high degree of directionality. The ion beam is well-collimated, allowing for precise control of the incidence angle and enabling highly anisotropic etching profiles. The angle of incidence strongly influences the sputtering yield and final etch profile, while tilted incidence angles may also lead to shadowing effects and redeposition of sputtered material on the sidewalls [73]. However, due to the absence of chemical selectivity, the etch rates of different materials are often similar, which can make selective etching challenging. In applications where selectivity between different materials becomes critical, chemically assisted etching techniques offer a good alternative. One such approach is microwave plasma etching, which will be discussed in the following section.

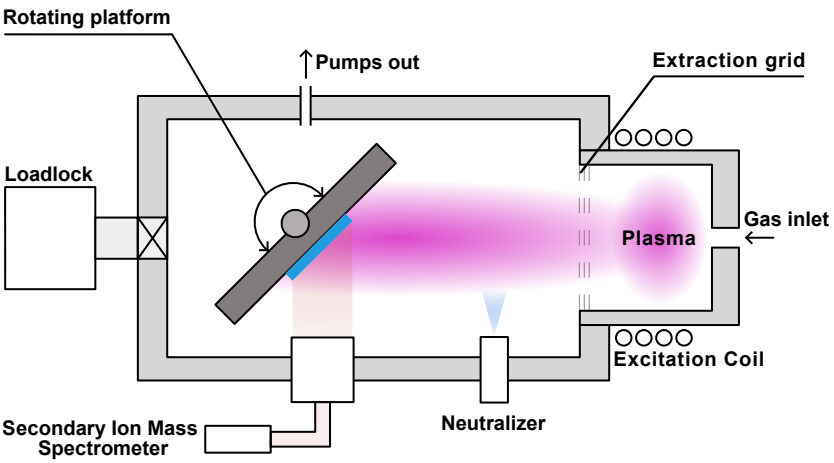


Figure 3.4: Schematic illustration of the ion beam etching (IBE) system. Ions generated in the plasma source are extracted and accelerated toward the substrate using an extraction grid, forming a directional ion beam. The energetic ions sputter material from the sample surface through momentum transfer, enabling highly anisotropic material removal. A neutralizer is used to compensate charge accumulation during the etching process, while a secondary ion mass spectrometer (SIMS) can be employed for in-situ monitoring of the sputtered species and process control.

3.3.3 Microwave etching

Microwave plasma treatment represents a low-damage plasma-based dry processing technique commonly used for surface cleaning and activation. In these systems, plasma is generated by microwave radiation, typically at frequency 2.45 GHz. The process is carried out in vacuum chamber where a process gas (commonly oxygen or argon) is introduced and ionized by the microwave field. Unlike capacitively coupled plasma systems like RIE, microwave plasmas do not rely on an electrode bias, resulting in low ion energies and reduced ion bombardment. As a result, microwave plasma treatment is primarily driven by chemically reactive species and radicals rather than physical sputtering. This makes the technique particularly suitable for gentle surface cleaning, removal of organic contaminants and surface activation without significant damage to delicate nanostructures [74].

4. Results

In the following sections, the optimization of the fabrication process, the realization of free-standing bilayer metasurfaces, and the fabrication and optical characterization of a single-layer metapolarimeter are presented and discussed.

4.1 Optimization of fabrication

The primary motivation of this work was the fabrication of TiO_2 free-standing bilayer metasurfaces. However, since the bilayer fabrication process directly builds upon the single-layer fabrication approach, optimization of the individual fabrication steps was first carried out for single-layer structures. Establishing a reliable single-layer process was essential before extending the fabrication towards more complex multilayer architectures. The fabrication of the nanostructures involves a sequence of several steps, each of which plays an important role in the final structure quality. The workflow consists of spin-coating of the positive resist. Then electron-beam lithography (EBL) is used to define the nanostructure patterns followed by development of the exposed resist Into the patterned holes, TiO_2 is subsequently deposited using atomic layer deposition (ALD). Since ALD provides conformal coverage of the sample, ion beam etching (IBE) is used to remove the excess material. Finally, resist was removed using microwave etching in pure oxygen plasma. Schematically this process is illustrated in Figure 4.1. Optimization of each of these steps will is thoroughly described in the following text.

4.1.1 Preparation of samples

Since the metasurface should work in visible spectral region, substrate with suitable optical properties in this range had to be selected. Because many metasurfaces functions in transmission regime, 300μm silicon dioxide (SiO_2) was chosen as the substrate material due to its high transparency in the visible region [75]. The thickness of the substrate was not critical parameter and was mainly determined by wafer availability.

EBL presents several challenges related to the resist itself - poor adhesion to inorganic substrates [76, 77] and charge accumulation during exposure on dielectric

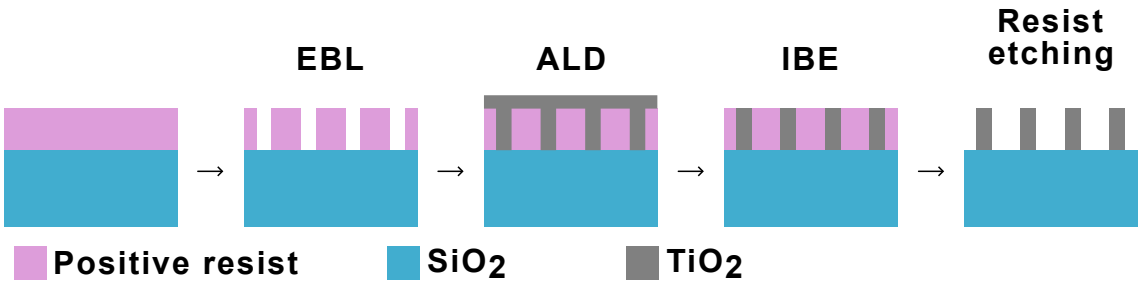


Figure 4.1: Schematic illustration of the fabrication process. From left to the right: spin-coating of the positive resist on a SiO_2 substrate, EBL patterning and development, ALD deposition of TiO_2, ion beam etching of the excess TiO_2 layer and resist removal to reveal the final nanostructures.

materials are among the most common [78]. To address these problems, an adhesion promoter and conductive coating were used in addition to the resist during spin-coating. Adhesion promoters are thin chemical layers applied to the substrate surface prior to resist coating, This improves the bonding between the resist and the substrate by modifying the surface chemistry to enhance wettability and adhesion. Generally, they are applied from vapor phase in an oven or as a liquid by spin-coating, depending on the specific used chemical. Throughout this work two adhesion promoters were used - AR 300-80 New from *Allresist*, a liquid promoter applied by spin-coating, and HMDS (hexamethyldisilazane), which is adhesion promoter deposited from vapors [79]. Initially, I used AR 300-80 New, which is applied by spin-coating for 1 minute at 4000 rpm followed by baking at 180°C. At this temperature, the promoter reacts with the substrate surface to form stable Si-O bonds, leaving a covalently bound hydrophobic monolayer that improves resist wetting and adhesion. The excess promoter is then removed by rinsing with acetone or isopropanol, while the monolayer remains intact. Later, I switched to HMDS, which works by bonding to the oxidized substrate surface and forming a hydrophobic layer, similarly improving resist adhesion, becuase it showed superior adhesion compared to AR 300-80 New. The summary of adhesion promoters and how they are applied is in Table 4.3.

As was stated in chapter introduction, positive resist is needed to create a mask for the subsequent ALD deposition. We can distinguish two main chemical groups of available positive resist: CSAR-based (chemical semi-amplified resist, based on polyα-methylstyrene-co-methyl chloroacrylate) and PMMA-based (polymethyl methacrylate) resists. Each was available in multiple concentrations, as summarized in Table 4.1.

Because resist layer directly defines the height of the fabricated nanostructures, the choice of resist thickness is critical parameter. High-aspect ratio nanostructure are desirable for metasurface applications, as taller structures provide greater phase accumulation. A target nanostructure height of 500 nm was selected as reasonable

Table 4.1: Overview of the e-beam resist materials considered for the fabrication process, including their chemical type, product label, achievable thickness range, developer and corresponding product datasheet.

Chemical type	Resist	Thickness range	Developer	Information
PMMA-based	950K AR-P 679.02	60–120 nm	AR 600-56	[80]
	950K AR-P 679.04	220–630 nm	AR 600-56	[80]
	600K AR-P 669.04	180–460 nm	AR 600-56	[80]
CSAR-based	AR-P 6200.13	350–720 nm	AR 600-546	[81]
	AR-P 6200.04	80–250 nm	AR 600-546	[81]

compromise between phase control and fabrication feasibility, requiring a resist capable of forming layer of at least this thickness. Based on these requirements, two candidates were chosen: the PMMA-based resist 950K AR-P 679.04 and the CSAR-based resist AR-P 6200.13 from *Allresist*. According to the manufacturers' datasheets, both resist should produce layers in the required thickness range at specific spin-coating speeds. In my case resist thickness was an important parameter as it directly determined the height of the fabricated nanostructures, making it necessary to get as close to 500 nm as possible. For this reason, I used a spectroscopic reflectometer *Ocean Optics NanoCalc 2000* to determine the real thickness of the resist on spin-coating speed. This method is suitable because both resists are sufficiently transparent under visible light, allowing fast and reliable thickness measurements [82]. However, this method requires a reflective substrate so the test samples were prepared on the polished silicon samples rather than SiO_2 substrates.

It should be noted right away that the IBE step, which is used to remove the excessive TiO_2 layer deposited on top of the resist, inevitably etches a certain amount of the resist itself. Based on experience with this process, approximately 40–50 nm of already exposed layer is consumed during IBE. This must be taken into account when selecting the resist thickness, which should therefore exceed the target nanostructure height by at least this margin. For the PMMA-based 950K AR-P 679.04, a spin-coating speed of 1400 rpm for 1 minute was selected, yielding a thickness of approximately 530 nm. Although this is slightly below the ideal margin, lower spin speeds resulted in poor homogeneity across the substrate surface, making 1400 rpm the best compromise between thickness and uniformity. For the CSAR-based resist AR-P 6200.13, a spin-coating speed of 2700 rpm for 1 minute was selected, yielding a thickness of approximately 554 nm with good homogeneity across the surface. Both resists were subsequently soft-baked on a hotplate to remove residual solvent and improve adhesion to the substrate [83]. For 950K AR-P 679.04, a bake at 150°C for 3 minutes was used, while AR-P 6200.13 was baked at 150°C for 2 minutes, following manufacturers recommendations. In the bilayer fabrication process, AR-P 6200.13 was primarily selected as the bottom resist layer,

Table 4.2: Summary of spin-coating settings, resulting resist thicknesses, and softbake parameters for the two electron beam resists used in this work

	Spin-coating settings	Thickness	Softbake parameters
950K AR-P 679.04	1400 rpm for 1 min	530 nm	150°C for 3 min
AR-P 6200.13	2700 rpm for 1 min	554 nm	150°C for 2 min

while PMMA-based 950K 679.04 was selected as the top layer. This decision came from fact that the CSAR-based resist are usually better during longer processing, because they have better thermal stability. For better overview, the spin-coating parameters are summarized in the Table 4.2.

As mentioned before, charge accumulation during electron beam exposure is another common issue in EBL, particularly on dielectric substrates such as SiO_2. To mitigate this, a conductive layer can be applied on top of the resist. One approach is to deposit a thin metal film, such as titanium or chromium by physical vapor deposition. However, this requires an additional deposition and etching step. An alternative is to use a conductive polymer coating, such as AR-PC 5092.02 (or Electra 92), which can be simply spin-coated on top of the resist and removed by rinsing with deionized water before development. Due to its simpler application, Electra 92 was used in this work. It was spin-coated at 2500 rpm for 1 minute, yielding a thickness of approximately 45 nm according to the datasheet, followed by baking on hotplate at 90°C for 2 minutes to get rid of the residual solvent. The adhesion promoters and conductive coating used in this work, along with their application method, are summarized in Table 4.3.

Table 4.3: Overview of the additional chemicals used during spin-coating, including adhesion promoters and conductive coatings, along with their application method and corresponding product datasheet.

Type	Material	Application	Product information
Adhesion promoter	HMDS	vapor deposition in oven	[84]
	AR 300-80 New	spin-coating	[83]
Conductive coating	AR-PC 5092.02	spin-coating	[85]
	Ti, Cr	physical vapor deposition	

At the beginning of the optimization process, a simple test metasurface design was used. The test metasurface consisted of arrays of rectangular nanostructures with varying lateral dimensions ranging from $300\times300\,nm^2$ down to $40\times40\,nm^2$ with step of 20 nm in both lateral directions, while the periodicity was fixed at 500 nm. Metasurface is $200\times200\,\mu m^2$ and the arrays in the metasurfaces are $10\times10\,\mu m^2$. The structure was primarily used for optimization of the fabrication process and evaluation of the quality of the achieved fabrication. The relatively simple geometry also enabled significantly shorter EBL exposure times, making the structure more

suitable for optimization of the fabrication parameters. Schematic of the tester metasurface is shown in Figure 4.2.

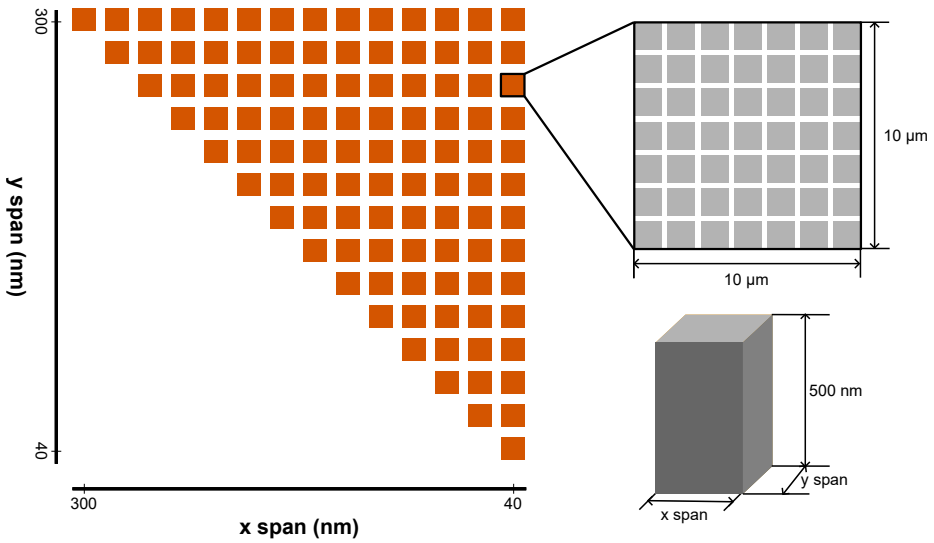


Figure 4.2: Test metasurface design used for fabrication process optimization, consisting of arrays of rectangular nanostructures with lateral dimensions ranging from $300\times300\,\mathrm{nm}^2$ down to $40\times40\,\mathrm{nm}^2$ with step size 20 nm. The periodicity was fixed at 500 nm.. The inset shows a detailed view of a single array with dimensions of $10\times10\,\mu\mathrm{m}^2$, and the right panel shows a schematic of an individual nanostructure with target height 500 nm.

The EBL exposures were performed using and scanning electron microscope (SEM) *TESCAN Mira3* equipped with the electron-beam writer *Raith ELPHY*. An acceleration voltage of 30 kV was used during exposures, as this voltage provides the smallest spot size on this system. This acceleration voltage is also highest possible acceleration machine can achieve. An exposure dose of $160\mu\mathrm{C/cm}^2$ was used. This dose was determined empirically, as initial dose $100\mu\mathrm{C/cm}^2$ proved insufficient, yielding no visible pattern after development. Finally for the write field size, I used write field with size $100\times100\mu\mathrm{m}^2$. This is a small write field, however, considering the design I used, its size is reasonable. This small write field enables more accurate patterning within each field, but comes at the cost of increased stitching between adjacent fields.

The stitching of the write fields presents a problem for patterning of the continuous structures such as waveguides [86], where even small alignment errors yields to discontinuities that hinder the overall waveguide functionality. In the case of metasurfaces, however, slight stitching errors on the order of several nanometers, typically around 10-20,nm for the *TESCAN Mira3* system, are not expected to significantly influence the resulting structures. This is mainly because metasurfaces consist of periodic arrays of spatially separated nanostructures that enhance and alter the light locally. Therefor small positional deviations within the array due to the stiching error has only a minor influence on the overall functionality.

Consequently, the use of multiple stitched write fields did not lead to noticeable degradation of the fabricated patterns.

After EBL exposure, the samples were developed in order to remove exposed regions of the positive resist. Prior to development, the samples were rinsed in deionized water to remove the conductive layer Electra 92 used during the exposure. Subsequently, the samples were immersed in developer AR 600-546 for 2 minutes [87]. After development, the samples were transferred into isopropyl alcohol, which served to stop further development. The developed resist with pattern subsequently served as a template for the conformal TiO_2 deposition performed by ALD.

Throughout this work, two ALD machines were used. Initially, depositions were performed using *Atomic layer deposition systems Ultratech/Cambridge NanoTech Fiji 200*. Since the nanostructures are fabricated within the developed resist, the deposition temperature had to be kept sufficiently low to prevent the resist from exceeding its glass transition temperature over long time.

After exceeding the glass transition temperature, the resist undergoes structural changes that can compromise the pattern profile or prevent its complete removal after processing. For AR-P 6200.13 the glass transition temperature is around 148°C, while AR-P 679.04 has glass transition temperature lower around 105°C.

Fiji features a large chamber, which, while versatile, results in significantly longer deposition times. Since we deposit material directly on the resist, plasma-enhanced ALD is unacceptable, as the reactive radicals from plasma could directly react with resist damaging the pattern. For this reason thermal ALD was selected. Specifically low-temperature recipe for deposition of TiO_2, which was developed and kindly provided to me by Ing. Ondřej Červinka. Deposition takes place at temperature of 90°C, and uses tetrakis(dimethylamido)titaniumm (TDMAT) and H_2O as precursors, with pulse time of 400 ms and purge time of 10 s for TDMAT, and pulse time of 200 ms and purge time of 7 s for H_2O. The expected deposition rate was ≈ 0.74 Å per cycle, based on Ondřej's previous work [88]. To verify the parameters, two test depositions were performed at 2300 and 3000 cycles, yielding layers of approximately 280 nm and 350 nm, corresponding to deposition rates of 123 Åand 116 Å per cycle, respectively. The thickness measurements were carried out by me using spectroscopic reflectometry and also by my friend Bc. Radim Slovák using spectroscopic ellipsometry on *J.A. Woollam RC2 Mapping Spectroscopic Ellipsometer*. The high deposition rate also compromise the quality of the deposited layer, since unusually high growth rates in ALD may indicate departure from the ideal self-limiting growth regime and the presence of parasitic chemical vapor deposition-like reactions, which can negatively affect film uniformity and material quality [89]. The initial hypothesis was that the TDMAT precursor was nearly depleted, which can cause irregular deposition behavior. After consulting with the machine guarantor, it was decided to switch to second ALD system, as my

hypothesis was not correct and the issue could not be reliably resolved on the *Fiji*.

The second machine used was *Beneq TFS 200*, a system with a compact chamber, which results in considerably shorter deposition times compared to the *Fiji*. There, I used general user ALD recipe for deposition of TiO_2 at 90°C $TiCl_4$ and H_2O as precursors, with pulse and purge times of 150 ms and 3 s for $TiCl_4$ and 150 ms and 5 s for H_2O, respectively. The deposition was performed again at 90°C. Similarly, two test depositions were performed first at 2500 and 3000 cycles, yielding 125.4 nm and 152 nm, corresponding to deposition rates of 0.5 Å and 0.51 Å per cycle, respectively. These were measured using only spectroscopic reflectometry. Unlike the *Fiji*, these values are in excellent agreement with each expected deposition rate for this recipe on this machine and consistent, confirming reliable and consistent deposition behavior.

An important advantage of using ALD for this process is its suitability for high-aspect-ratio nanostructures. Since ALD growths conformally, the height of the deposited nanostructures is not determined by the deposition itself, but rather by the lateral dimensions of the holes defined during EBL. As illustrated in Figure 4.3, when the layer grows on the walls of the holes, the effective opening gradually narrows until the holes are completely filled. Therefore, for the largest lateral dimensions in my tester metasurface of $300 \times 300\,\mu m^2$, a minimum deposition of 150 nm was required to ensure complete filling. Since 3000 cycles yielded thickness of 152 nm, which leaves virtually no margin, 3100 cycles were used in order to ensure complete filling. It should be noted that the process also deposits a continuous layer on top of the resist, which cannot be removed by standard lift-off process and therefore requires something like IBE.

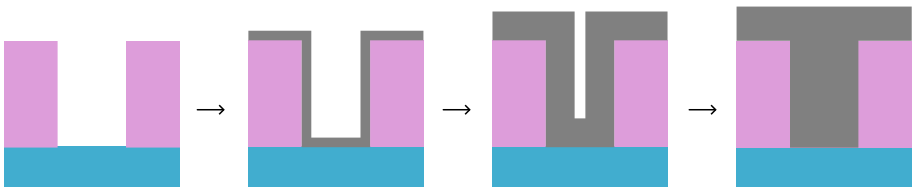


Figure 4.3: Schematic illustration of the conformal TiO_2 atomic layer deposition into patterned resist holes, illustrating the progressive filling of the nanostructures and formation of a continuous layer on top of the resist.

The excess TiO_2 layer deposited on top of the resist was removed by IBE using the *SCIA Systems Coat 200*. The etching was performed at tilt angle 60° with a sample rotation of 10 rpm, which improves etch uniformity and minimizes redeposition onto the sidewalls of the nanostructures. The ion beam source was operated at 300 W with an acceleration voltage of 400 V and beam voltage of 400 V, these parameters were established from previous experience with this system and are known to provide reliable etching results for this type of process. Backside helium cooling was applied at flow rate of 10 sccm to prevent excessive heating of the sample during etching.

The etch endpoint was monitored using secondary ion mass spectrometry (SIMS), which detects changes in the secondary ion signal as the etching transitions between materials [90], allowing precise determination of when the top TiO_2 layer is fully removed. An additional 60 s of etching was performed after the endpoint was confirmed to ensure complete removal. The process was then finished with extra 1 minute etch at a reduced tilt of 40° to remove material redeposited during the main etching step. Endpoint detection signal is shown in Figure 4.4. As we can see there are three types of titanium signals, due to titanium having more naturally occuring isotopes, in SIMS this is used to increase reliability. The signal remained stable for approximately 19 minutes, after which it began to drop, indicating that the conformal TiO_2 layer was being cleared. Once the signal reached a count rate of approximately 1000-10000, an additional 1 minute of etching was performed to ensure complete removal before terminating process. From the etch duration and the known layer thickness, the etch rate was estimated to be approximately 6.52 nm/min. Unfortunately, at the start of May the turbomolecular pump of the endpoint detection system failed, rendering the SIMS unavailable for the remainder of the experimental work. For the subsequent samples, the etch duration was therefore estimated based on this established etch rate.

Resist removal proved to be one of the most challenging steps in the fabrication process. In general, two approaches can be used for the resist removal: wet etching

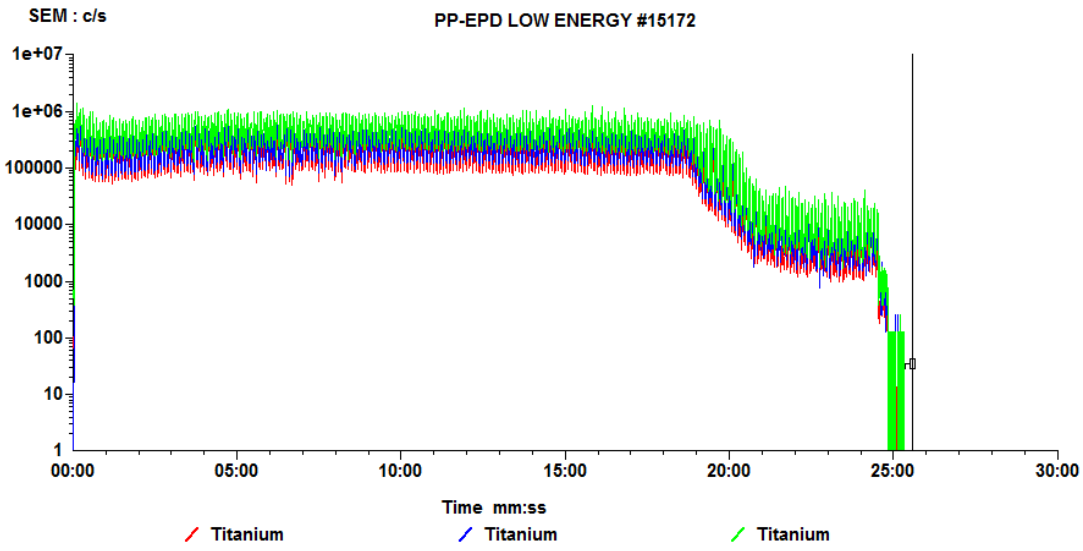


Figure 4.4: SIMS signal recorded by the endpoint detection system during IBE of TiO_2 excessive layer. The three traces correspond to different titanium secondary ion signals, due to titanium naturally occuring in more isotopes, are monitored throughout the process. The signal remains approximately constant in first 19 minutes, followed by dropping indicating removal of layer. At minute 25 the process was terminated. The y-axis in logarithmic scale.

and dry etching techniques. For wet removal, dioxolane AR 600-71 was considered, since it is compatible with both PMMA- and CSAR-based resists. However, this approach presented several practical disadvantages. First, the wet etching process is relatively slow. More importantly, the fabricated high-aspect-ratio nanostructures were expected to be mechanically fragile after the removal process. Since wet processing is typically followed by drying using nitrogen, there was concern, that drying could deform or collapse the fabricated nanostructures. For this reason, plasma-based resist removal was investigated as an alternative approach. In this process, the organic polymer resist reacts with oxygen (O_2) plasma and is gradually removed, while the TiO_2 nanostructures remain unaffected due to their significantly higher chemical stability against O_2 plasma. Initially, RIE was attempted using the *Oxford Instruments PlasmaPro 80*, with pure O_2 plasma, to ensure removal of only resist. The set parameters were O_2 at flow rate of 30 sccm, pressure of 100 mTorr and RF power of 50 W. The higher pressure was chosen to decrease free mean path of ions, thus decreasing the ion bombardment of the subtrate surface, while the RF power was set as low while still reliably striking and maintaining the plasma. While this successfully removed the resist, the process was way too aggressive and caused the nanostructures to collapse. We can see that in Figure 4.5.

Reducing the RF power to 10 W improved the situation while still maintaining a stable plasma, however the self-bias remained at 72 V indicating that the process was not purely chemical and still contained a significant ion bombardment. While test arrays showed promising results with well-defined upright nanostructures, applying the same parameters to the metapolarizer design, about which I will talk later, the

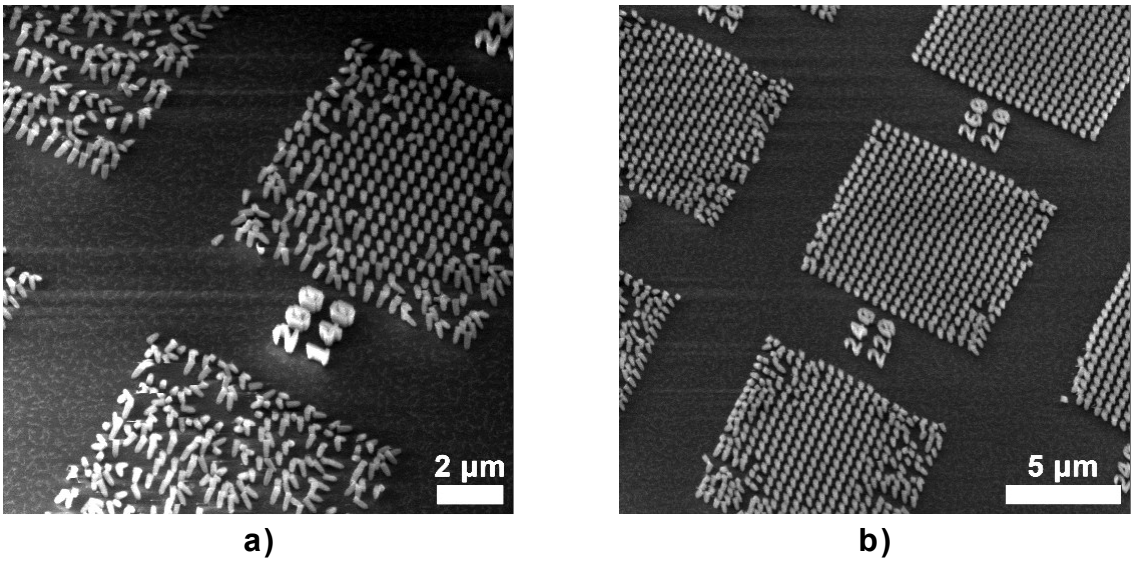


Figure 4.5: Applying adhesion promoter AR 300-80 New improved the fabrication of TiO_2 nanostructures. (a,b) SEM images showing that while the adhesion promoter prevented the structures from collapsing, the RIE resist removal process still caused visible damage to the nanostructures, particularly at the array edges.

design revealed that the process was still not sufficiently gentle - localized collapse of the nanostructures was observed in some areas of the array, as shown in Figure 4.6.

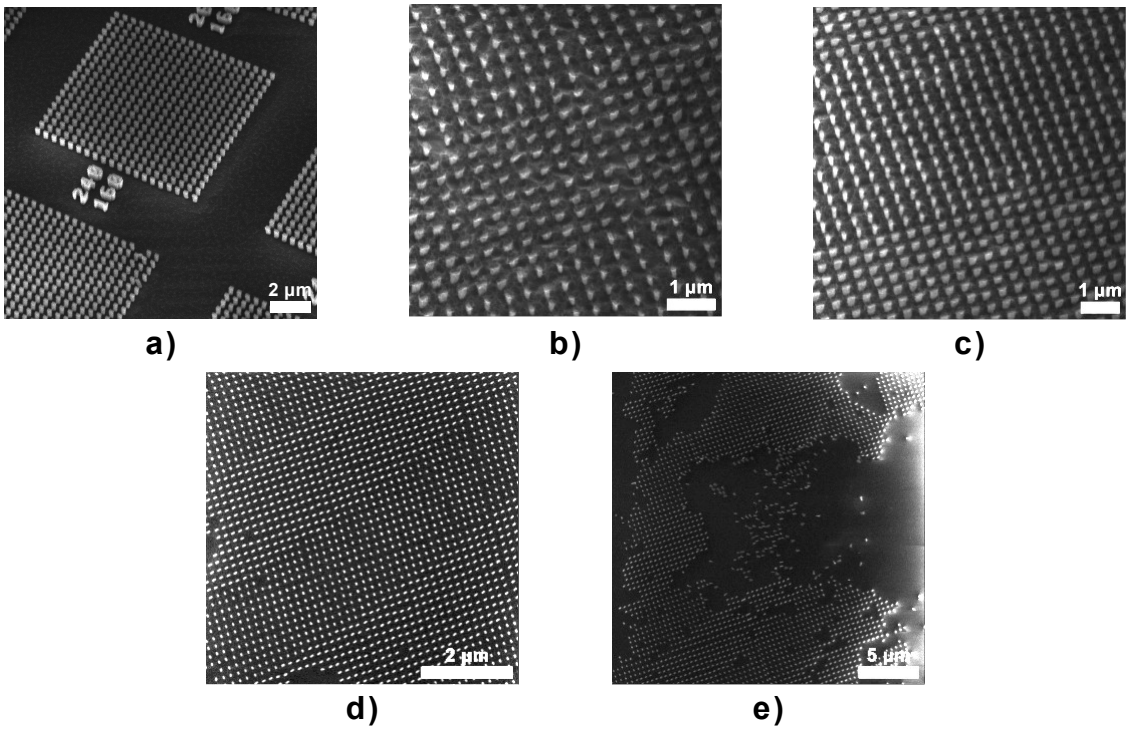


Figure 4.6: Effect of RF power reduced to 10 W on resist removal using RIE. SEM image of the test array (a) showing promising results with well-defined upright nanostructures. However, when the same parameters were applied to the metapolarizer design (b–e), localized collapse of the nanostructures was still observed in some areas of the array.

This confirmed that RIE was not suitable for this process and a different approach was needed, thus I switched to a microwave plasma cleaner, the *Diener Electronic NANO*, which operates without a DC bias and therefore provides a gentler, purely chemical etching. At this stage, the adhesion promoter was also changed from AR 300-80 New to HMDS, based on the recommendation of other users that HMDS provides superior adhesion. Using pure O_2 plasma at 80 % power, the resist was successfully removed after approximately two hours and the nanostructures survived the process cleanly, as shown in Figure 4.7.

4.1.2 Bilayer metasurface fabrication

After optimization of the process for single layer metasurface an attempt was made to fabricate a free-standing bilayer TiO_2 metasurface, inspired by the architecture demonstrated by Dorrah et al.[58], In this configuration, two layers of TiO_2 nanostructures are vertically stacked, with air as the surrounding medium, providing high refractive index contrast and reduced parasitic reflections.

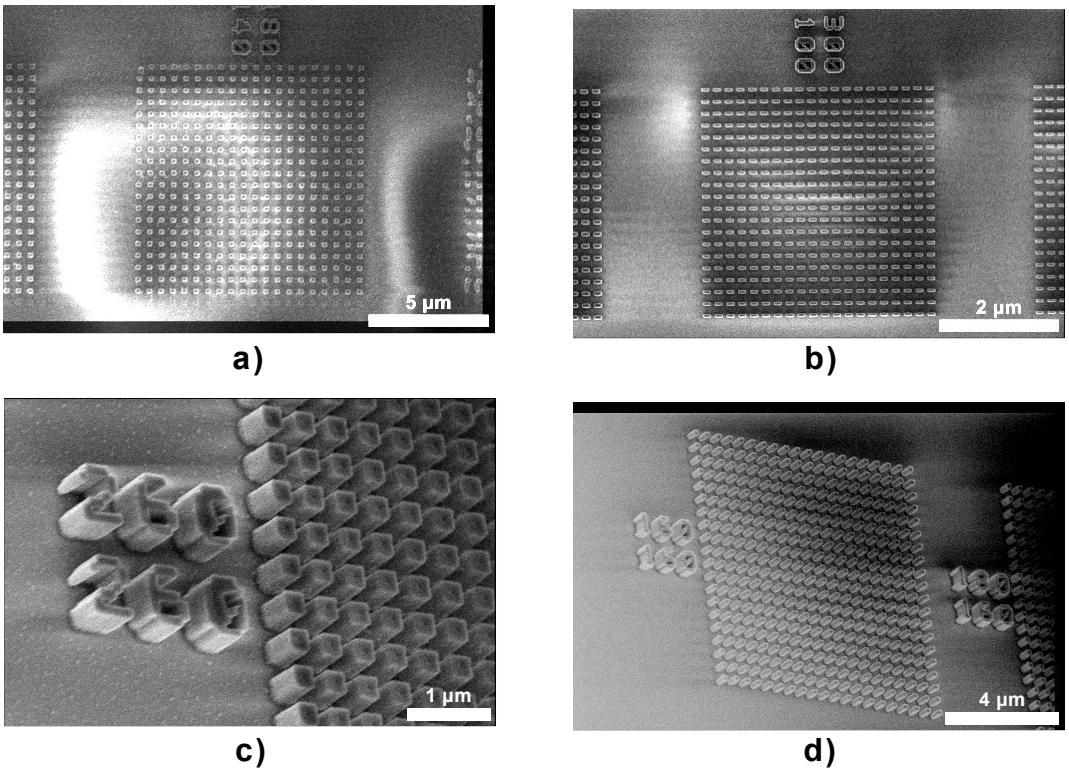


Figure 4.7: Successfully fabricated TiO_2 nanostructures arrays after switching to HMDS as the adhesion promoter and O_2 microwave etching for resist removal. SEM images showing well-defined, high-aspect-ratio nanostructures in lateral sizes (a,b), as well as detailed views confirming the structural integrity and uniformity of the individual nanopillars (c,d).

The fabrication of such structure follows the same sequence as the single-layer process, repeated twice. The key to enabling this bilayer approach lies in the selective development between two resist layers. During the second EBL exposure, part of the electron beam penetrates into the underlying resist due to electron scattering effects. However, by using resist layers that respond differently to the corresponding development processes, the upper exposed layer can be selectively developed while preserving the underlying layer and the already fabricated nanostructures. This selective development is important because it preserves the already fabricated first layer during the second processing step. Schematically this process is shown in Figure 4.8.

There, CSAR was used as the first layer resist and PMMA as the second. After completing the full single-layer fabrication - spin-coating, EBL, development, ALD and IBE - a second resist, as well as conductive coating is spin-coated directly on top, followed by a second EBL exposure and development. Since PMMA and CSAR respond to different developers, the second development step selectively attacks only the PMMA layer without affecting the underlying CSAR, preserving the integrity of the first layer structures. A second ALD and IBE step then defines the second layer

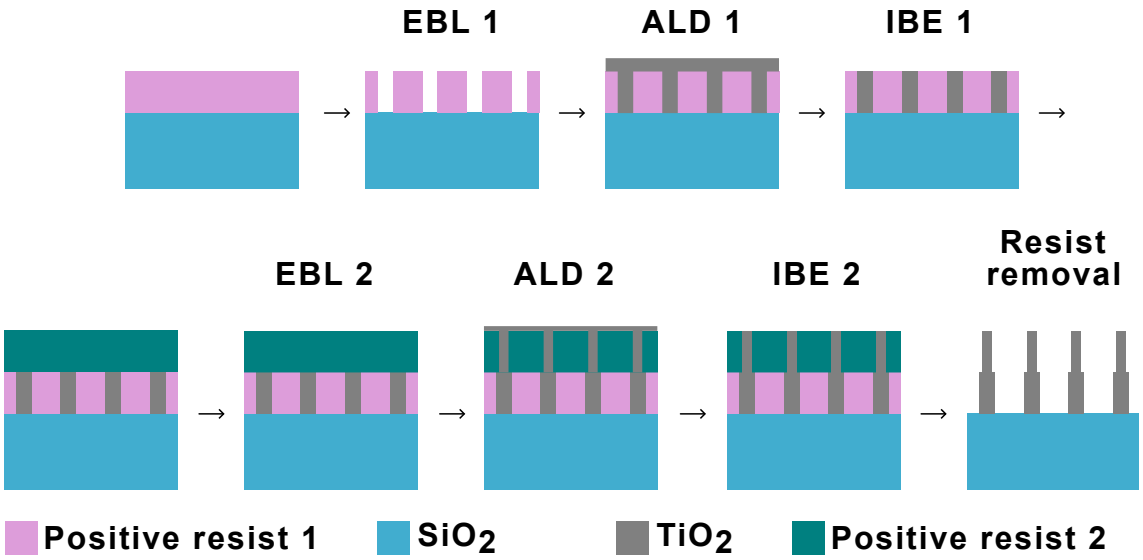


Figure 4.8: Schematic illustration of the free-standing bilayer metasurface fabrication process consiting of two sequention EBL-ALD-IBE cycles using selective development between the two resist layers. Final resist removal reveals the free-standing bilayer nanostructures surrounded by air.

of nanostructures, and finally both resist layers are removed together, leaving the free-standing bilayer TiO_2 nanostructures surrounded by air. Despite this elegant approach, the critical challenge lies in the precise alignment of the second EBL exposure, with respect to the first layers, as any misalignment directly affects the optical performance of the device.

To test feasibility of the bilayer fabrication process, a dedicated test metasurface was designed and fabricated using the optimized TiO_2 process described in the previous chapter. The metasurface consisted of two layers of rectangular TiO_2 nanostructures, each layer composed of 16×16 matrix of arrays, where each individual array contained 20×20 nanostructures with period of 500 nm, corresponding to a 10×10 μm^2. The top layer consisted of a sweep of rectangular nanostructures dimensions ranging from 250×250 nm^2 in steps of 10 nm, while the bottom layer was kept fixed at 300×300 nm^2 throughout. To evaluate the overlay alignment accuracy between the two EBL exposures, the entire metasurface was replicated in a 5×5 matrix, where each copy had a predefined lateral offset of -20, -10, 0, +10, +20 nm between the top and bottom layers in both directions, with the central structure corresponding to zero offset. This was in retrospective really low offset, to be even noticeable.

Global and local alignment markers were used during second EBL exposure in order to minimize overlay errors between the two fabrication steps. While the global markers enabled coarse sample alignment, the local markers were used for fine alignment in the vicinity of the metasurface structures. A write field size of

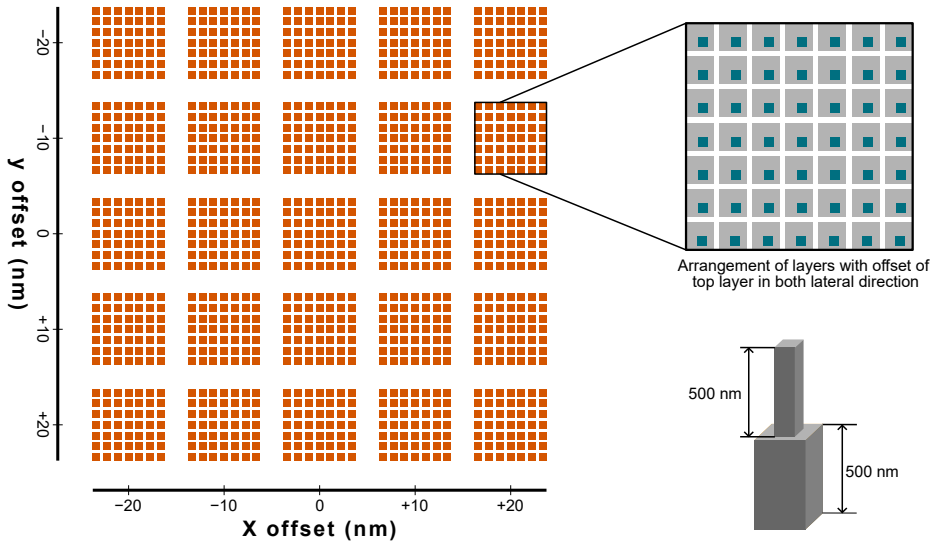


Figure 4.9: Schematic illustration of the fabricated bilayer metasurface test structures. The left panel shows the 5×5 matrix of metasurfaces with intentionally introduced lateral offsets between the top and bottom layers ranging from -20 nm to 20 nm in both x and y directions. The central structure corresponds to zero relative offset.

$100\times100\,\mu m^2$ was selected, and the alignment marks were sized accordingly. The global and local alignment marks, where in a shape of crosses for focusing with a length of both arms of 50 μm and 10 μm, respectively.

An important consideration for the bilayer process is the material of the alignment marks, which must remain visible through the second resist layer during the second EBL exposure. Initially, several materials were tested for this purpose, including gold and chromium. While gold is particularly well suited due to its strong secondary electron signal, its deposition requires an additional processing step. It was later realized that the TiO_2 marks defined during the first EBL exposure and subsequent ALD step provide sufficient contrast for alignment in the second exposure, eliminating the need for any additional mark deposition step.

Exposure parameters were chosen for each resist layer independently. For AR 6200.13, an exposure dose of $160\,\mu m/cm^2$ was used. Following exposure, the conductive coating Electra 92 was rinsed off with deionzied water, and the resist was developed in AR 600-546 fpr 2 minutes, followed by 30 second stop in isopropanol. After development, the already established process - 3000 cycles of ALD TiO_2 deposition followed by IBE to remove the excessive material from the surface, completing the first nanostructure layer.

For the second layer, a 950K AR-P 679.04 was used. Since the target nanostructure height was kept at 500 nm for both layers, a spin-coating recipe of 14000 rpm for 1 minute was used, yielding a thickness of approximately 530 nm. A conductive coating was again applied on top of the resist prior to exposure. The

exposure dose was set to $350\,\mu C/cm^2$, which is a typical dose for PMMA, that can be found in datasheets. After exposure of second layer, conductive coating was rinsed off with deionized water, and the resist was developed in AR 600-56 -a different developer compared to the CSAR process. The subsequent steps followed the same procedure as established for the first layer. Final structures can be seen in Figure 4.10.

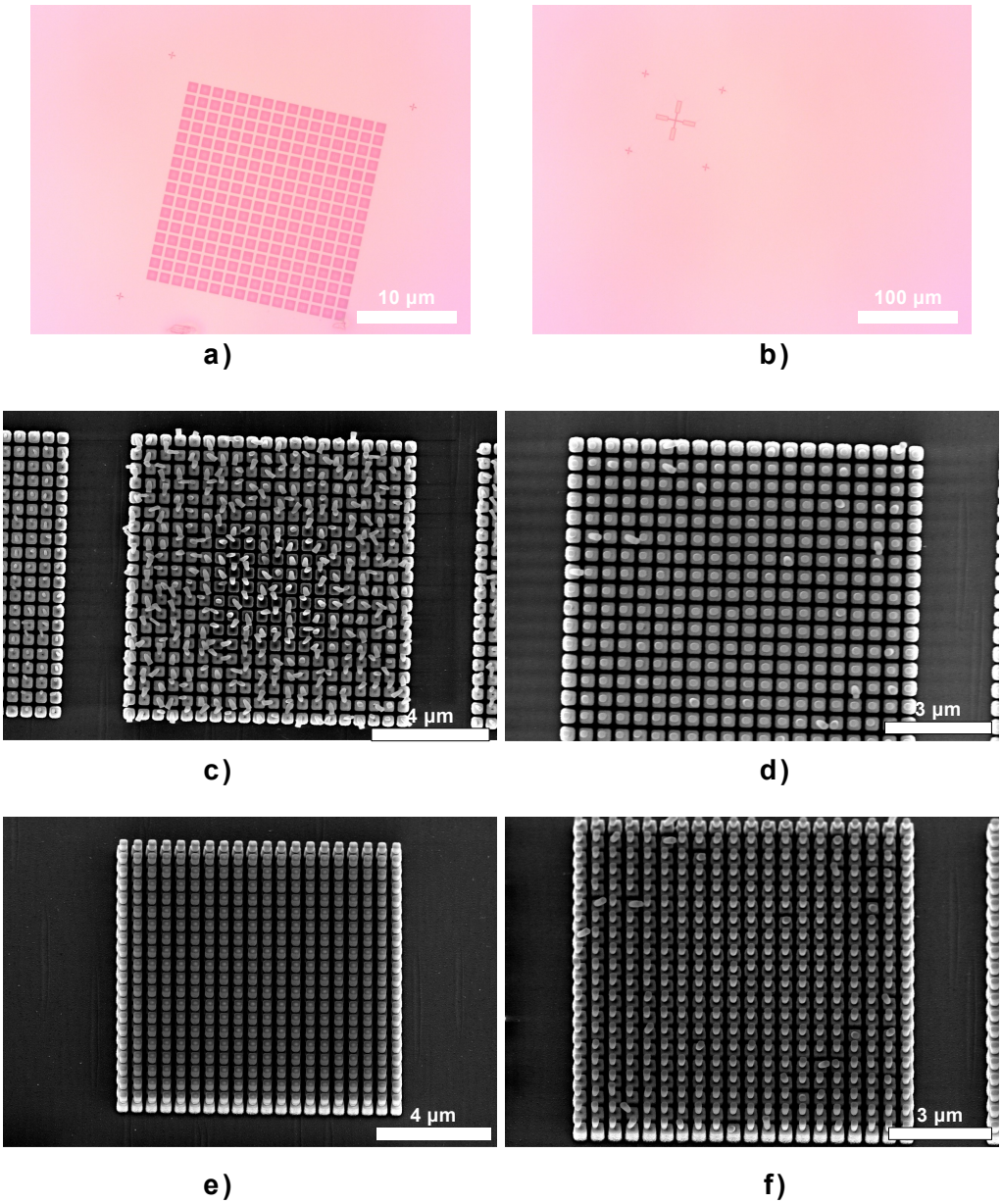


Figure 4.10: optical microscope and SEM images of the fabricated free-standing bilayer metasurface structures. a) Optical microscope image of the fabricated metasurface array with local marks around it for precise alignment. b) Optical microscope image of the global alignment marker used during the second EBL exposure. c) SEM image of collapsed bilayer nanostructures with smaller lateral dimensions, illustrating the limitations of the current fabrication process for dense high-aspect-ratio structures. d) top-view SEM image of a bilayer metasurface composed of square nanoposts. e) SEM image of larger bilayer rectangular nanofins exhibiting good structural stability and definition. f) SEM image of another bilayer nanofin array with larger lateral dimensions, where the rounded shape and reduced lateral definition of the structures can be observed.

Despite the fact that the fabrication process was not fully optimized for smaller structures yet, the bilayer structures fabricated using the selective development process were successfully realized and exhibit good structural stability. The

fabricated nanostructures withstood the final resist removal step without significant deformation or collapse, demonstrating the feasibility of the developed free-standing bilayer fabrication approach. Moreover, the SEM images confirmed that the fabricated structures closely matched the intended designs, and even these first fabrication attempts yielded highly promising results. Further optimization of the exposure conditions, particularly for the PMMA resist layer, is expected to improve the definition of the smallest features even further.

4.2 Metapolarimeter

As the fabrication of the bilayer metasurface proved to be a time-consuming and technically demanding process, a decision was made in parallel to fabricate a single-layer advanced metasurface - metapolarimeter based on design of Ing. Martin Hrtoň, Ph.D.

4.2.1 Design and fabrication

While simpler from a fabrication standpoint, this device represents and advanced metasurface design, combining two optical functions within a single device - a metalens with focal point in 2 mm and waveplate with retardation of $3\pi/4$. The metasurface consists of rectangular TiO_2 nanofins with target height of 500 nm and periodicity of 500 nm as well. The design consists of two nanofins geometries: $214\times80\,nm^2$ and $164\times90\,nm^2$. The metalens focuses incident light through a spatially varying phase profile, while the waveplate functionality is achieved by rotating the rectangular nanofins across the metasurface. The device was optimized for operation at wavelength of 532 nm in transmission regime. The combination of these two function produces a characteristic polarization-dependent point spread function (PSF) in the focal plane allowing the Stokes parameters to be determined for an arbitrary input polarization state. The detail theoretical background of this design is beyond the scope of this thesis. Schematically you can see the design in Figure 4.11.

Optimized process parameter in previous chapter enabled the successful fabrication of the this metapolarimeter, yielding well-defined, high-aspect ratio TiO_2 nanostructures as shown in Figure 4.12. The process used AR-P 6200.13 as a electron beam lithography resist. Based on the SEM characterization, the previously empirically selected exposure dose of $160\mu m/cm^2$ provided good overall pattern fidelity. This metapolarimeter was subsequently measured to evaluate its optical functionality. It should be noted that the final nanostructure height was approximately 450 nm instead of the intended 500 nm. During the fabrication of this metasurface, endpoint detection set up was at this point unavailable. Lateral

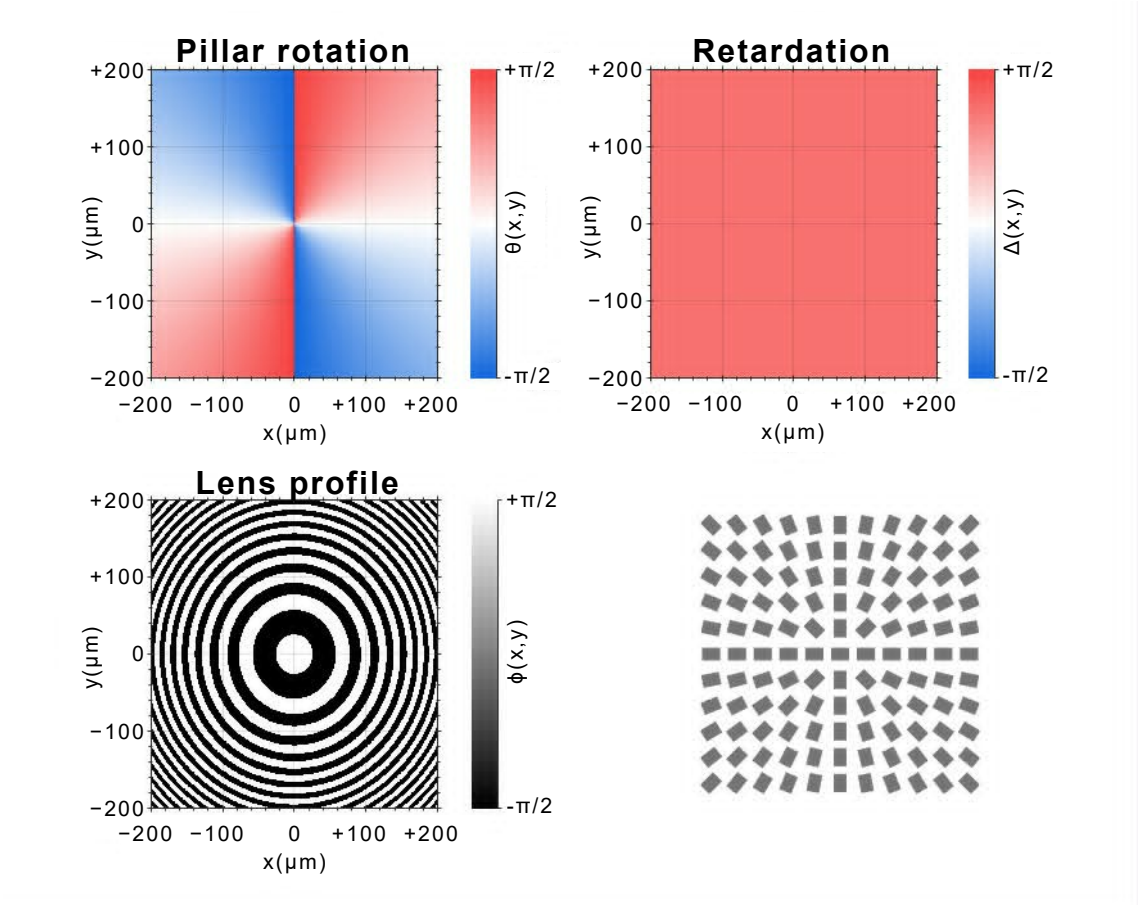


Figure 4.11: Design of the metapolarimeter metasurface by Ing. Martin Hrtoň, Ph.D. Top left: spatial distribution of the nanofin rotation angle θ(x,y) across the metasurface. Top right: corresponding retardation map Δ(x,y) showing a uniform retardation of $3\pi/4$. Bottom left: lens phase profile ϕ(x,y) encoding the metalens functionality. Bottom right: illustration of the resulting nanofin arrangement showing the spatially varying rotation of the rectangular nanofins.

dimensions where also a bit bigger. Individual meta-atoms, instead of $214\times80\,\mathrm{nm}^2$ and $164\times90\,\mathrm{nm}^2$, the lateral sizes around $236\times100\,\mathrm{nm}^2$ and $186\times135\,\mathrm{nm}^2$. Later we will see that on overall functionality of the metasurface, this error in lateral dimensions did not have significant influence.

4.2.2 Optical measurements

Polarimetry is an optical technique used for characterization of the polarization state of light. Since polarization carries important information about the optical field and its interaction with matter, polarimetric measurements are widely used in optics microscopy and imaging applications [91]. One of the most used descriptions of polarizations is the Stokes formalism, in which the polarization state of light is represented by four Stokes parameters collected into the Stokes vector [52, p. 388]

$$\mathbf{S} = (s_0, s_1, s_2, s_3). \tag{4.1}$$

Here s_0 corresponds to the total intensity of light, while s_1, s_2, s_3 describe the polarization state. Specifically, s_1 represents intensity difference between horizontal and vertical polarization, s_2 between diagonal polarization states, and s_3 between right- and left-circular polarization states. For fully polarized light, the stokes parameters satisfy the relation

$$s_0^2 = s_1^2 + s_2^2 + s_3^2, \tag{4.2}$$

which allows the polarization state to be represented geometrically on the Poincaré sphere. In this representation, linear polarization states lie along the equator of the sphere, while right- and left-circular polarization states correspond to the north and south poles, respectively. Elliptically polarized states occupy intermediate positions depending on their ellipticity and orientation.

Conventionally, the Stokes parameters are determined through several sequential measurements using combinations of polarizers and wave plates [92, p. 104]. Similarly, metasurface-based polarimeter, presented in this work, carries polarization

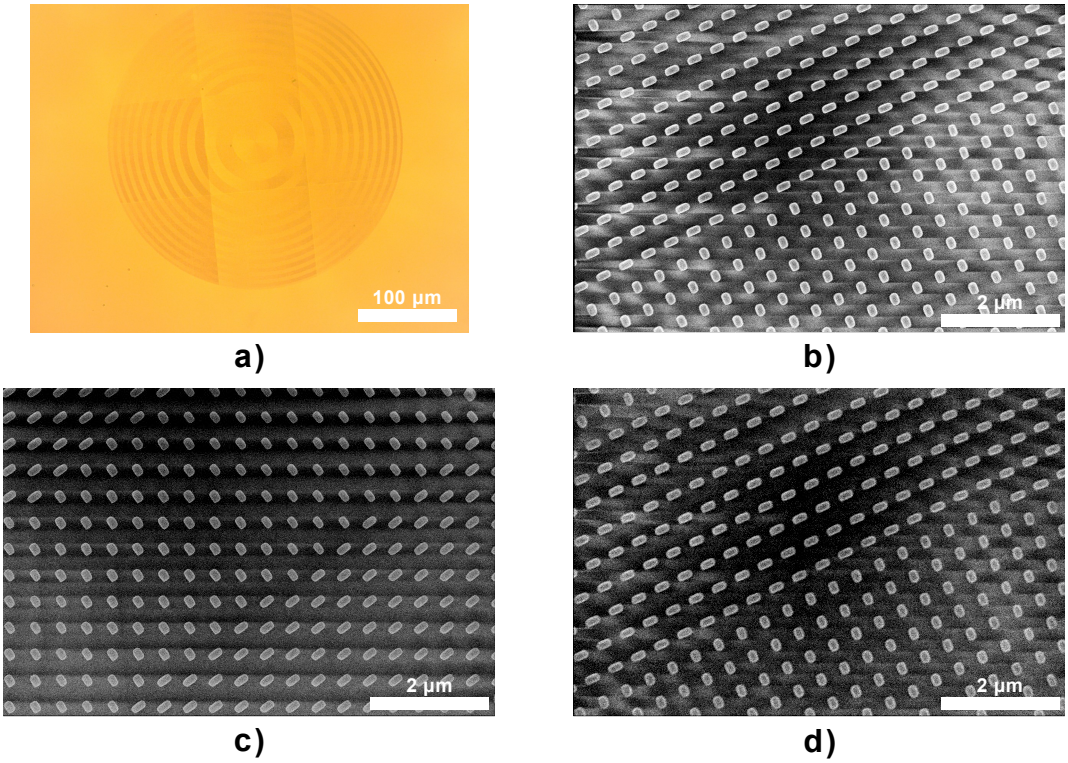


Figure 4.12: Successfully fabricated metapolarimeter. a) optical microscope image of the full metasurface, showing the Fresnel-like profiles across the 300 μm aperture. (b–d) SEM images revealing well-defined, high aspect ratio TiO_2 nanofins with clearly resolved spatial variation in their rotation across the metasurface.

information directly into the PSF in the focal plane - anisotropic nanofins interacts differently with orthogonal polarization components of the incident light, thus the transmitted optical field becomes polarization dependent. At the same time, the metalens phase profile causes the transmitted field to interfere in the focal plane, producing a polarization-dependent PSF. Different incident polarization states therefore generate characteristic intensity distributions, from which the corresponding Stokes parameters can be subsequently reconstructed.

The optical characterization of the fabricated metapolarimeter was carried out with assistance of my supervisor Ing. Petr Viewegh, Ph.D. The optical setup used for characterization of the metapolarimeter is schematically shown in Figure 4.13. A 532 nm laser beam is focused into a single-mode optical fibre using an objective lens. The fibre output produces a coherent spherical wave by a second objective lens. The collimated beam then passes through a polarizing beam splitter, which transmits horizontally polarized light, defining the initial polarization state of the beam. The polarization state is then controlled using a combination of half-wave plate and quarter-wave plate. The half-wave plate allows manipulation of linear polarization states along the equator of the Poincaré sphere, while the quarter-wave plate enables conversion between linear, elliptical and circular polarization states, allowing any arbitrary polarization state to be prepared.

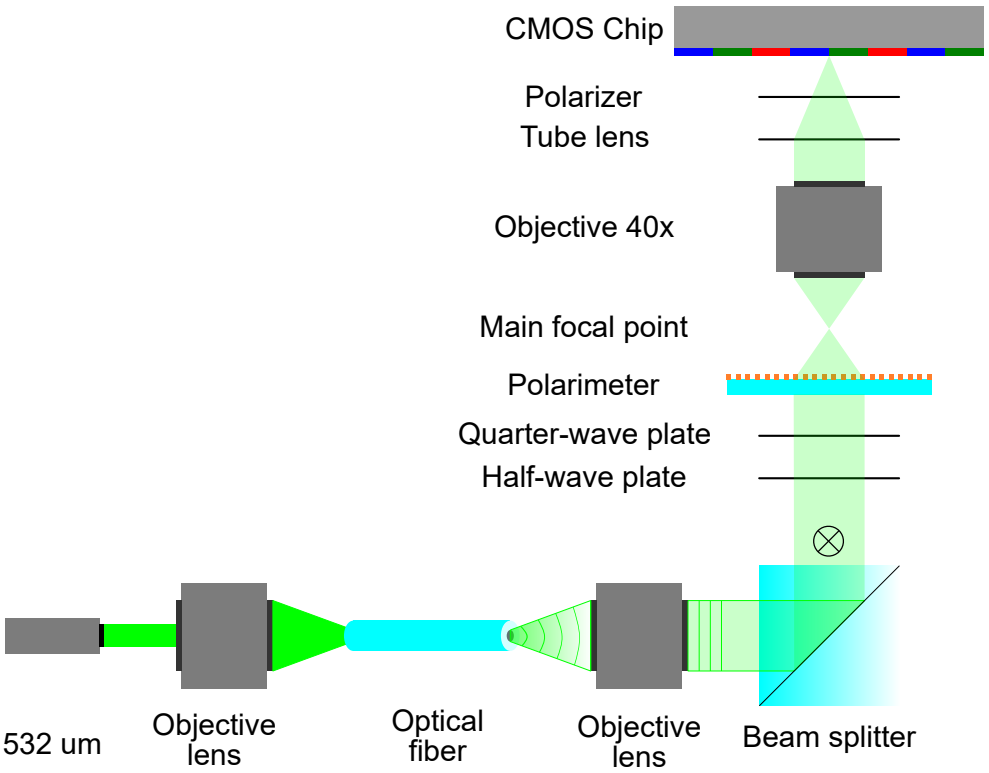


Figure 4.13: Schematic of the experimental setup used for metapolarimeter characterization.

The prepared beam then illuminates the metapolarimeter, whose metalens

component focuses the light to a main focal point. The focused beam is then collected by 40× magnification objective lens and directed through a tube lens. A linear polarizer placed before the camera CMOS chip is used to distinguish between horizontal and vertical polarization components. The resulting polarization-dependent PSF is finally projected onto the camera chip, from which the Stokes parameters of the incident beam can be determined.

During the measurements, the intensity distributions generated by the metasurface in the focal plane were recorded for various input polarization states. Representative PSF obtained for selected polarization states are shown in Figure 4.14, alongside the corresponding theoretically predicted intensity distributions. As expected, the spatial intensity distribution of the PSF changed with the incident polarization state, confirming the polarization-sensitive response of the fabricated metapolarimeter.

While the qualitative agreement between the measured and theoretically predicted PSFs is clearly visible, a direct visual comparison alone is insufficient for rigorous quantification of the polarimetric performance. The complex and spatially varying nature of the PSF make it difficult to extract Stokes parameters from the measured intensity distributions. To address this, a neural network developed and trained by Ing. Ondřej Červinka was employed. The network

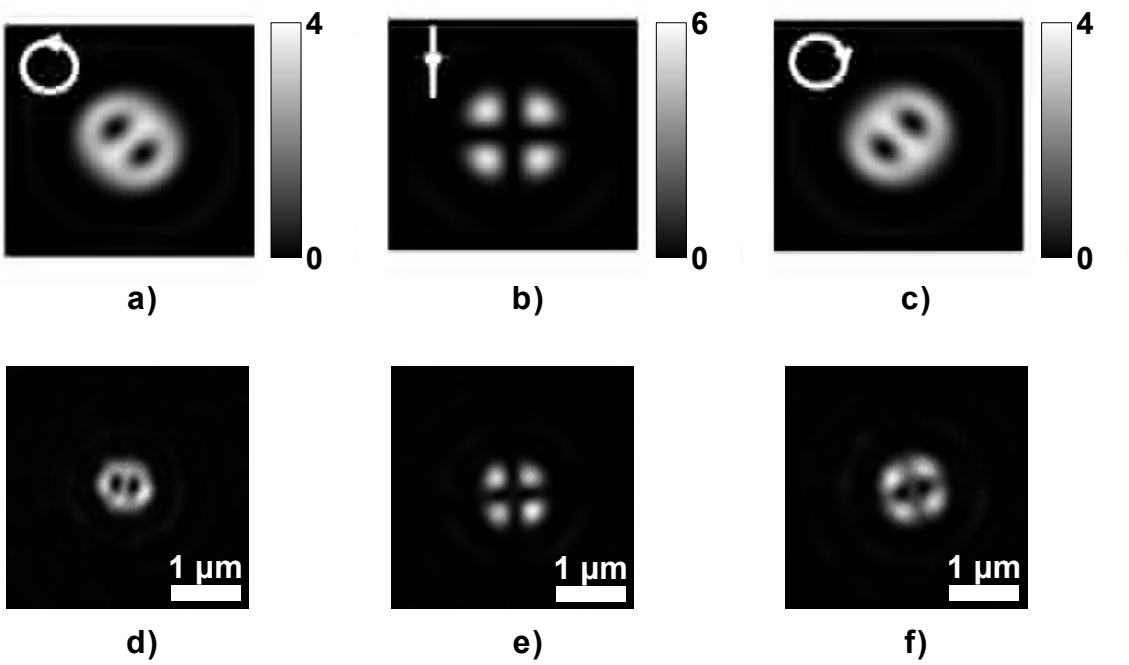


Figure 4.14: Theoretically predicted (a–c) and experimentally measured (d–f) point spread functions of the fabricated metapolarimeter for selected input polarization states: left-circular polarization (a, d), linear vertical polarization (b, e), and right-circular polarization (c, f). The characteristic two-lobe and four-spot intensity distributions reflect the polarization-dependent response of the device, with good qualitative agreement observed between experiment and theory.

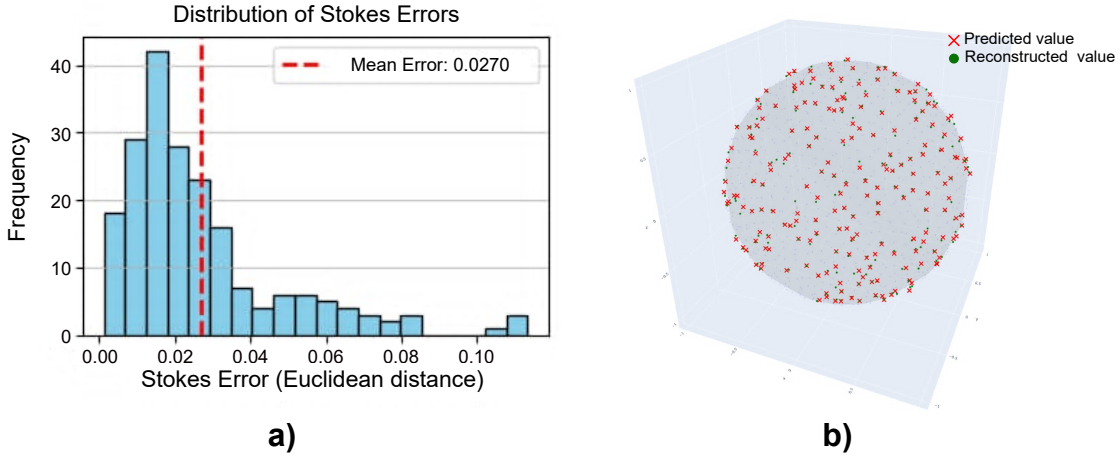


Figure 4.15: (a) Distribution of the Stokes parameter reconstruction error represented by the Euclidean distance, with the dashed line indicating the mean error. (b) Visualization of the reconstructed polarization states on the Poincaré sphere compared to the predicted values.

was trained on theoretically calculated PSFs and subsequently applied to the experimentally measured intensity distributions, comparing the measured PSFs against the theoretical predictions to extract the corresponding Stokes parameters. This allowed the polarimetric accuracy of the fabricated device to be quantified through the Stokes error metric, the results of which are presented in Figure 4.15. The histogram shows the distribution of measurement errors across a set of 200 input polarization states, where the error determines how closely the measured polarization state matches the theoretically expected one.

The relative deviation between theory and experiment ranges from 0 to 0.11, although on average the deviation is only 0.027. This is satisfying result and it confirms that the fabricated metapolarimeter successfully reproduces the expected polarization-dependent response, demonstrating the optical functionality.

Conclusion

The goal of this thesis was to fabricate and characterize advanced optical metasurfaces based on TiO_2 nanostructures. The experimental work was focused on two main objectives: developing a reliable fabrication process for free-standing bilayer metasurfaces, and demonstrating a functional advanced single-layer metasurface device.

The fabrication process was optimized step by step, starting from single-layer structures. The CSAR-based resist AR-P 6200.13 was selected as the primary resist due to its better thermal stability, than PMMA based 950K AR-P 679.04. HMDS proved superior to the liquid adhesion promoter AR 300-80 New in terms of nanostructure stability, and Electra 92 was used to mitigate charge accumulation during EBL on the dielectric SiO_2 substrate. Reliable ALD deposition was established on the Beneq TFS 200 system at a consistent rate of approximately 0.5 Å per cycle at 90°C. The most critical challenge was the resist removal - reactive ion etching caused collapse of the nanostructures even at reduced power, and the problem was resolved by switching to a microwave plasma cleaner, which provided sufficiently gentle purely chemical etching using O_2 plasma.

Building on the optimized single-layer process, we successfully fabricated the first free-standing bilayer TiO_2 metasurfaces. The approach relies on selective development between CSAR and PMMA resist layers, allowing the second fabrication cycle to be carried out without disturbing the already fabricated first layer. We found that TiO_2 alignment markers from the first cycle provide sufficient contrast for alignment of the second EBL exposure, eliminating the need for additional metallic marker deposition. The fabricated bilayer structures showed good mechanical stability and closely matched the intended designs, representing a promising first result.

In parallel, a single-layer metapolarimeter combining metalens and waveplate functionality was fabricated and optically characterized at 532 nm. Despite slight deviations in the final nanostructure dimensions from the design targets, Stokes parameter reconstruction using a neural network yielded a mean error of only 0.027 across 200 measured polarization states, confirming the successful optical functionality of the device.

Future work should focus on systematic optimization of the PMMA exposure

conditions to improve the dimensional fidelity of the bilayer structures, and on extending the process toward bilayer devices with full optical functionality.

Overall, both goals of this thesis were successfully achieved. A reliable fabrication process for TiO_2 metasurfaces was established and free-standing bilayer metasurfaces were realized, alongside a functional metapolarimeter with demonstrated optical performance. The road to these results was far from straightforward - numerous technical setbacks were encountered along the way, from equipment failures to collapsing nanostructures. However, as Albert Einstein once said, "Anyone who has never made a mistake has never tried anything new."

List of Abbreviations

ALD	Atomic Layer Deposition
CMOS	Complementary Metal-Oxide Semiconductor
CSAR	Chlorinated Styrene Acrylate Resist
EBL	Electron Beam Lithography
HMDS	Hexamethyldisilazane
IBE	Ion Beam Etching
PB	Pancharatnam-Berry
PMMA	Polymethyl Methacrylate
PSF	Point Spread Function
RF	Radio Frequency
RIE	Reactive Ion Etching
SEM	Scanning Electron Microscope
SIMS	Secondary Ion Mass Spectrometry
SiO_2	Silicon Dioxide
TDMAT	Tetrakis(dimethylamido)titanium
$TiCl_4$	Titanium Tetrachloride
TiO_2	Titanium Dioxide

List of References

[1] H.-T. Chen, A. J. Taylor, and N. Yu. "A review of metasurfaces: physics and applications". In: *Reports on progress in physics* 79.7 (2016), p. 076401.

[2] M. Khorasaninejad, W. T. Chen, R. C. Devlin, J. Oh, A. Y. Zhu, et al. "Metalenses at visible wavelengths: Diffraction-limited focusing and subwavelength resolution imaging". In: *Science* 352.6290 (2016), pp. 1190–1194.

[3] D. N. Neshev and A. E. Miroshnichenko. "Enabling smart vision with metasurfaces". In: *Nature Photonics* 17.1 (2023), pp. 26–35.

[4] A. Arbabi and A. Faraon. "Advances in optical metalenses". In: *Nature Photonics* 17.1 (2023), pp. 16–25.

[5] D. Neshev and I. Aharonovich. "Optical metasurfaces: new generation building blocks for multi-functional optics". In: *Light: Science & Applications* 7.1 (2018), p. 58.

[6] J. Jung, H. Park, J. Park, T. Chang, and J. Shin. "Broadband metamaterials and metasurfaces: a review from the perspectives of materials and devices". In: *Nanophotonics* 9.10 (2020), pp. 3165–3196.

[7] W. Zhu, F. Xiao, M. Kang, and M. Premaratne. "Coherent perfect absorption in an all-dielectric metasurface". In: *Applied Physics Letters* 108.12 (2016).

[8] I. Staude, A. E. Miroshnichenko, M. Decker, N. T. Fofang, S. Liu, et al. "Tailoring directional scattering through magnetic and electric resonances in subwavelength silicon nanodisks". In: *ACS nano* 7.9 (2013), pp. 7824–7832.

[9] L. Liu, X. Zhang, M. Kenney, X. Su, N. Xu, et al. "Broadband metasurfaces with simultaneous control of phase and amplitude". In: *Advanced materials* 26.29 (2014), pp. 5031–5036.

[10] G.-Y. Lee, G. Yoon, S.-Y. Lee, H. Yun, J. Cho, et al. "Complete amplitude and phase control of light using broadband holographic metasurfaces". In: *Nanoscale* 10.9 (2018), pp. 4237–4245.

[11] Y. Intaravanne and X. Chen. “Recent advances in optical metasurfaces for polarization detection and engineered polarization profiles”. In: *Nanophotonics* 9.5 (2020), pp. 1003–1014.

[12] Y. Deng, Z. Cai, Y. Ding, S. I. Bozhevolnyi, and F. Ding. “Recent progress in metasurface-enabled optical waveplates”. In: *Nanophotonics* 11.10 (2022), pp. 2219–2244.

[13] N. Yu and F. Capasso. “Flat optics with designer metasurfaces”. In: *Nature materials* 13.2 (2014), pp. 139–150.

[14] M. Rasool and S. M. Abbas. “Applications of Metasurfaces in Beam Steering Systems”. In: *physica status solidi (a)* 223.5 (2026), e202500841.

[15] S. Wang, P. C. Wu, V.-C. Su, Y.-C. Lai, M.-K. Chen, et al. “A broadband achromatic metalens in the visible”. In: *Nature nanotechnology* 13.3 (2018), pp. 227–232.

[16] M. L. Tseng, H.-H. Hsiao, C. H. Chu, M. K. Chen, G. Sun, et al. “Metalenses: advances and applications”. In: *Advanced Optical Materials* 6.18 (2018), p. 1800554.

[17] Z.-B. Fan, H.-Y. Qiu, H.-L. Zhang, X.-N. Pang, L.-D. Zhou, et al. “A broadband achromatic metalens array for integral imaging in the visible”. In: *Light: Science & Applications* 8.1 (2019), p. 67.

[18] G. Zheng, H. Mühlenbernd, M. Kenney, G. Li, T. Zentgraf, et al. “Metasurface holograms reaching 80% efficiency”. In: *Nature nanotechnology* 10.4 (2015), pp. 308–312.

[19] X. Ni, A. V. Kildishev, and V. M. Shalaev. “Metasurface holograms for visible light”. In: *Nature communications* 4.1 (2013), p. 2807.

[20] D. Wen, F. Yue, G. Li, G. Zheng, K. Chan, et al. “Helicity multiplexed broadband metasurface holograms”. In: *Nature communications* 6.1 (2015), p. 8241.

[21] A. Pors, M. G. Nielsen, G. D. Valle, M. Willatzen, O. Albrektsen, et al. “Plasmonic metamaterial wave retarders in reflection by orthogonally oriented detuned electrical dipoles”. In: *Optics letters* 36.9 (2011), pp. 1626–1628.

[22] J. Wang and J. Du. “Plasmonic and dielectric metasurfaces: design, fabrication and applications”. In: *Applied Sciences* 6.9 (2016), p. 239.

[23] J. Parsons, E. Hendry, C. P. Burrows, B. Auguié, J. R. Sambles, et al. “Localized surface-plasmon resonances in periodic nondiffracting metallic nanoparticle and nanohole arrays”. In: *Physical Review B—Condensed Matter and Materials Physics* 79.7 (2009), p. 073412.

[24] N. Yu, P. Genevet, M. A. Kats, F. Aieta, J.-P. Tetienne, et al. “Light propagation with phase discontinuities: generalized laws of reflection and refraction”. In: *science* 334.6054 (2011), pp. 333–337.

[25] Y. Zhao and A. Alù. “Manipulating light polarization with ultrathin plasmonic metasurfaces”. In: *Physical Review B—Condensed Matter and Materials Physics* 84.20 (2011), p. 205428.

[26] J. Zhang, M. ElKabbash, R. Wei, S. C. Singh, B. Lam, et al. “Plasmonic metasurfaces with 42.3% transmission efficiency in the visible”. In: *Light: Science & Applications* 8.1 (2019), p. 53.

[27] A. Pors, M. G. Nielsen, R. L. Eriksen, and S. I. Bozhevolnyi. “Broadband focusing flat mirrors based on plasmonic gradient metasurfaces”. In: *Nano letters* 13.2 (2013), pp. 829–834.

[28] H.-H. Hsiao, C. H. Chu, and D. P. Tsai. “Fundamentals and applications of metasurfaces”. In: *Small Methods* 1.4 (2017), p. 1600064.

[29] P. Genevet, F. Capasso, F. Aieta, M. Khorasaninejad, and R. Devlin. “Recent advances in planar optics: from plasmonic to dielectric metasurfaces”. In: *Optica* 4.1 (2017), pp. 139–152.

[30] M. Li, M. Liu, Y. Chen, Z.-D. Hu, J. Wu, et al. “All-dielectric metasurface lenses for achromatic imaging applications”. In: *Nanoscale Research Letters* 17.1 (2022), p. 81.

[31] S. Sun, Z. Zhou, C. Zhang, Y. Gao, Z. Duan, et al. “All-dielectric full-color printing with TiO2 metasurfaces”. In: *ACS nano* 11.5 (2017), pp. 4445–4452.

[32] H. Zhou, Z. Xing, Y. Hu, H. Gao, Z. Lin, et al. “Compact Generation of Ultraviolet Structured Light via Low-Loss Dielectric Metasurfaces”. In: *Advanced Optical Materials* 14.7 (2026), e01940.

[33] N. K. Emani, E. Khaidarov, R. Paniagua-Domínguez, Y. H. Fu, V. Valuckas, et al. “High-efficiency and low-loss gallium nitride dielectric metasurfaces for nanophotonics at visible wavelengths”. In: *Applied Physics Letters* 111.22 (2017).

[34] J. Yang and J. A. Fan. “Analysis of material selection on dielectric metasurface performance”. In: *Optics express* 25.20 (2017), pp. 23899–23909.

[35] J. Li, T. Wu, W. Xu, Y. Liu, C. Liu, et al. “Mechanisms of 2π phase control in dielectric metasurface and transmission enhancement effect”. In: *Optics Express* 27.16 (2019), pp. 23186–23196.

[36] J. Sautter, I. Staude, M. Decker, E. Rusak, D. N. Neshev, et al. “Active tuning of all-dielectric metasurfaces”. In: *ACS nano* 9.4 (2015), pp. 4308–4315.

[37] Z. Zhou, J. Li, R. Su, B. Yao, H. Fang, et al. “Efficient silicon metasurfaces for visible light”. In: *Acs Photonics* 4.3 (2017), pp. 544–551.

[38] S. M. Kamali, A. Arbabi, E. Arbabi, Y. Horie, and A. Faraon. “Decoupling optical function and geometrical form using conformal flexible dielectric metasurfaces”. In: *Nature communications* 7.1 (2016), p. 11618.

[39] N. Mahmood, I. Kim, M. Q. Mehmood, H. Jeong, A. Akbar, et al. “Polarisation insensitive multifunctional metasurfaces based on all-dielectric nanowaveguides”. In: *Nanoscale* 10.38 (2018), pp. 18323–18330.

[40] Y. Kivshar and A. Miroshnichenko. “Meta-optics with Mie resonances”. In: *Optics and Photonics News* 28.1 (2017), pp. 24–31.

[41] Y. F. Yu, A. Y. Zhu, R. Paniagua-Domínguez, Y. H. Fu, B. Luk’yanchuk, et al. “High-transmission dielectric metasurface with 2π phase control at visible wavelengths”. In: *Laser & Photonics Reviews* 9.4 (2015), pp. 412–418.

[42] M. Kerker, D.-S. Wang, and C. Giles. “Electromagnetic scattering by magnetic spheres”. In: *Journal of the Optical Society of America* 73.6 (1983), pp. 765–767.

[43] A. J. Ollanik, J. A. Smith, M. J. Belue, and M. D. Escarra. “High-efficiency all-dielectric Huygens metasurfaces from the ultraviolet to the infrared”. In: *ACS photonics* 5.4 (2018), pp. 1351–1358.

[44] E. Hasman, V. Kleiner, G. Biener, and A. Niv. “Polarization dependent focusing lens by use of quantized Pancharatnam–Berry phase diffractive optics”. In: *Applied physics letters* 82.3 (2003), pp. 328–330.

[45] L. Huang, H. Mühlenbernd, X. Li, X. Song, B. Bai, et al. “Broadband Hybrid Holographic Multiplexing with Geometric Metasurfaces.” In: *Advanced Materials (Deerfield Beach, Fla.)* 27.41 (2015), pp. 6444–6449.

[46] E. Cohen, H. Larocque, F. Bouchard, F. Nejadsattari, Y. Gefen, et al. “Geometric phase from Aharonov–Bohm to Pancharatnam–Berry and beyond”. In: *Nature Reviews Physics* 1.7 (2019), pp. 437–449.

[47] Q. Zhou, M. Liu, W. Zhu, L. Chen, Y. Ren, et al. “Generation of perfect vortex beams by dielectric geometric metasurface for visible light”. In: *Laser & Photonics Reviews* 15.12 (2021), p. 2100390.

[48] Z. Ma, Y. Li, Y. Li, Y. Gong, S. A. Maier, et al. “All-dielectric planar chiral metasurface with gradient geometric phase”. In: *Optics express* 26.5 (2018), pp. 6067–6078.

[49] Z. Hu, T. Xu, R. Tang, H. Guo, and S. Xiao. “Geometric-phase metasurfaces: from physics to applications”. In: *Laser & Optoelectronics Progress* 56.20 (2019), p. 202408.

[50] M. Khorasaninejad and F. Capasso. “Metalenses: Versatile multifunctional photonic components”. In: *Science* 358.6367 (2017), eaam8100.

[51] B. E. A. Saleh and M. C. Teich. *Fundamentals of Photonics*. 3rd. Wiley, 2019. ISBN: 978-1-119-50687-4.

[52] E. Hecht. *Optics*. 5th. Harlow, England: Pearson Education Limited, 2017. ISBN: 978-1-292-09693-3.

[53] J. Hao, Y. Yuan, L. Ran, T. Jiang, J. A. Kong, et al. “Manipulating electromagnetic wave polarizations by anisotropic metamaterials”. In: *Physical review letters* 99.6 (2007), p. 063908.

[54] F. Wang, A. Chakrabarty, F. Minkowski, K. Sun, and Q.-H. Wei. “Polarization conversion with elliptical patch nanoantennas”. In: *Applied Physics Letters* 101.2 (2012).

[55] O. Avayu, E. Almeida, Y. Prior, and T. Ellenbogen. “Composite functional metasurfaces for multispectral achromatic optics”. In: *Nature communications* 8.1 (2017), p. 14992.

[56] Y. Zhou, I. I. Kravchenko, H. Wang, H. Zheng, G. Gu, et al. “Multifunctional metaoptics based on bilayer metasurfaces”. In: *Light: Science & Applications* 8.1 (2019), p. 80.

[57] L. Deng, Z. Li, Z. Zhou, Z. He, Y. Zeng, et al. “Bilayer-metasurface design, fabrication, and functionalization for full-space light manipulation”. In: *Advanced Optical Materials* 10.7 (2022), p. 2102179.

[58] A. H. Dorrah, J.-S. Park, A. Palmieri, and F. Capasso. “Free-standing bilayer metasurfaces in the visible”. In: *Nature Communications* 16.1 (2025), p. 3126.

[59] A. Palmieri, A. H. Dorrah, J. Yang, J. Oh, P. Dainese, et al. “Do dielectric bilayer metasurfaces behave as a stack of decoupled single-layer metasurfaces?” In: *Optics Express* 32.5 (2024), pp. 8146–8159.

[60] A. A. Tseng, K. Chen, C. D. Chen, and K. J. Ma. “Electron beam lithography in nanoscale fabrication: recent development”. In: *IEEE Transactions on electronics packaging manufacturing* 26.2 (2003), pp. 141–149.

[61] R. Pease. “Electron beam lithography”. In: *Contemporary Physics* 22.3 (1981), pp. 265–290.

[62] R. W. Johnson, A. Hultqvist, and S. F. Bent. “A brief review of atomic layer deposition: from fundamentals to applications”. In: *Materials today* 17.5 (2014), pp. 236–246.

[63] K.-E. Elers, T. Blomberg, M. Peussa, B. Aitchison, S. Haukka, et al. “Film uniformity in atomic layer deposition”. In: *Chemical Vapor Deposition* 12.1 (2006), pp. 13–24.

[64] M. Vos, A. Mackus, and W. Kessels. *Atomic Layer Deposition Process Development – 10 steps to successfully develop, optimize and characterize ALD recipes*. 2019.

[65] D. Andriukaitis and R. Anilionis. "Investigation of etching process in nano structures". In: *Elektronika ir elektrotechnika* 86.6 (2008), pp. 77–80.

[66] H. Jansen, H. Gardeniers, M. de Boer, M. Elwenspoek, and J. Fluitman. "A survey on the reactive ion etching of silicon in microtechnology". In: *Journal of micromechanics and microengineering* 6.1 (1996), pp. 14–28.

[67] G. S. Oehrlein. "Reactive-ion etching". In: *Physics Today* 39.10 (1986), pp. 26–33.

[68] M. Huff. "Recent advances in reactive ion etching and applications of high-aspect-ratio microfabrication". In: *Micromachines* 12.8 (2021), p. 991.

[69] F. Karouta. "A practical approach to reactive ion etching". In: *Journal of Physics D: Applied Physics* 47.23 (2014), p. 233501.

[70] N. Maluf, S. Chou, J. McVittie, S. Kuan, D. Allee, et al. "Effects of chromium on the reactive ion etching of steep-walled trenches in silicon". In: *Journal of Vacuum Science & Technology B: Microelectronics Processing and Phenomena* 7.6 (1989), pp. 1497–1501.

[71] O. Joubert, J. Pelletier, and Y. Arnal. "The etching of polymers in oxygen-based plasmas: A parametric study". In: *Journal of applied physics* 65.12 (1989), pp. 5096–5100.

[72] P. G. Glöersen. "Ion- beam etching". In: *Journal of Vacuum Science and Technology* 12.1 (1975), pp. 28–35.

[73] R. E. Lee. "Microfabrication by ion-beam etching". In: *Journal of Vacuum Science and Technology* 16.2 (1979), pp. 164–170.

[74] K. Suzuki, S. Okudaira, N. Sakudo, and I. Kanomata. "Microwave plasma etching". In: *Japanese Journal of Applied Physics* 16.11 (1977), p. 1979.

[75] H. M. Yadav and J.-S. Kim. "Fabrication of SiO2/TiO2 double layer thin films with self-cleaning and photocatalytic properties". In: *Journal of Materials Science: Materials in Electronics* 27.10 (2016), pp. 10082–10088.

[76] A. Kawai, H. Nagata, and H. A. Takata. "Adhesion between photoresist and inorganic substrate". In: *Japanese journal of applied physics* 30.1R (1991), p. 121.

[77] J. J. Bauer, G. Drescher, H. Silz, H. Frankenfeld, and M. Illig. "Surface tension and adhesion of photo-and electron-beam resists". In: *Advances in Resist Technology and Processing XIV*. Vol. 3049. SPIE. 1997, pp. 640–649.

[78] B. L. Thiel and M. Toth. “Secondary electron contrast in low-vacuum/environmental scanning electron microscopy of dielectrics”. In: *Journal of applied physics* 97.5 (2005).

[79] BenchChem. *The Principle of Hexamethyldisilazane (HMDS) as an Adhesion Promoter: A Technical Guide*. Accessed: 2025-05-20. 2025. URL: <https://pdf.benchchem.com/1203/The_Principle_of_Hexamethyldisilazane_HMDS_as_an_Adhesion_Promoter_A_Technical_Guide.pdf>.

[80] Allresist GmbH. *Produktinformation E-Beam Resist AR-P 630–670*. 2020.

[81] Allresist GmbH. *Product Information E-Beam Resist AR-P 6200*. 2023.

[82] Lasertec Corporation. *Principle of Spectroscopic Reflectometry*. Accessed: 2025-05-20. 2025. URL: <https://www.lasertec.co.jp/en/products/microscope/optelics_hybrid/principle/spectroscopic.html>.

[83] Allresist GmbH. *Product Information Adhesion Promoter AR 300-80 new*. 2024.

[84] BenchChem. *Application Notes and Protocols for Hexamethyldisilazane (HMDS) Vapor Deposition*.

[85] Allresist GmbH. *Product Information Protective Coating AR-PC 5090/5091*. 2023.

[86] A. L. Bogdanov, J. Lapointe, and J. H. Schmid. “Electron-beam lithography for photonic waveguide fabrication: Measurement of the effect of field stitching errors on optical performance and evaluation of a new compensation method”. In: *Journal of Vacuum Science & Technology B* 30.3 (2012).

[87] Allresist GmbH. *AR 600-50/51/55/56/546/548/549 Product Information*. <https://www.allresist.com/wp-content/uploads/sites/2/2020/03/AR600-50-51-55-56-546-548-549_english_Allresist_product_information.pdf>. Accessed: 2026.

[88] O. Červínka. “Aplikace metapovrchů pro strukturální zbarvení”. Vedoucí práce Tomáš Šikola. MA thesis. Brno: Vysoké učení technické v Brně, Fakulta strojního inženýrství, Ústav fyzikálního inženýrství, 2021.

[89] S.-Y. Ham, Z. Jin, S. Shin, M. Kim, M. Seo, et al. “Investigation of abnormally high growth-per-cycle in atomic layer deposition of Al2O3 using trimethylaluminum and water”. In: *Applied Surface Science* 571 (2022), p. 151282.

[90] N. P. Lockyer, S. Aoyagi, J. S. Fletcher, I. S. Gilmore, P. A. van der Heide, et al. “Secondary ion mass spectrometry”. In: *Nature Reviews Methods Primers* 4.1 (2024), p. 32.

[91] K. Singh, N. Tabebordbar, A. Forbes, and A. Dudley. “Digital Stokes polarimetry and its application to structured light: tutorial”. In: *Journal of the Optical Society of America A* 37.11 (2020), pp. C33–C44.

[92] D. Goldstein. *Polarized Light*. 2nd. New York: Marcel Dekker, Inc., 2003. ISBN: 0-8247-4053-X.